PREDICTION OF THE STRESS-STRAIN BEHAVIOR OF POLYCRYSTALLINE α-IRON CONTAINING HARD SPHERICAL PARTICLES

Russell H. Jones
(Ph. D. Thesis)

October 10, 1971

AEC Contract No. W-7405-eng-48

DISCLAIMER

Table of Contents

PREDICTION OF THE STRESS-STRAIN BEHAVIOR OF POLYCRYSTALLINE α-IRON CONTAINING HARD SPHERICAL PARTICLES

Russell H. Jones

Inorganic Materials Research Division, Lawrence Berkeley Laboratory and Department of Materials Science and Engineering, College of Engineering; University of California, Berkeley, California

ABSTRACT

The stress-strain behavior of polycrystalline α-iron containing hard spherical particles has been successfully predicted with relationships based on particle-dislocation interaction mechanisms. The yielding behavior obeyed a modified Orowan type relationship, as proposed by Ashby. The work hardening rates were in close agreement with the rates predicted by a model based on the generation of secondary dislocations at the particles, also proposed by Ashby. The objective of this study was to utilize these relationships, which were developed to predict the flow properties of single crystals containing hard particles, to predict the flow properties of polycrystals containing hard particles. Alloys with second phase volume fractions of 0.73 to 6.14% and particle diameters of 1250Å to 2300Å were examined. The distribution of the particle diameters and randomness of the particle dispersion were examined with carbon extraction replicas. The volume fraction of second phase was determined with the aid of the electron beam microprobe analyzer. The matrix structure was studied with optical and electron transmission microscopy and the grain orientation randomness was examined with the x-ray Laue back reflection technique.

I. INTRODUCTION

There has been much effort to derive relationships which describe the yielding behavior and work hardening behavior of single phase alloys. The yield strength has been related to dislocation morphology, alloy content, grain size, internal stresses, particle morphology and many other variables. Also, the work hardening of single phase alloys has been related to grain size, dislocation density and stacking fault energy.

In two phase alloys containing hard particles the largest amount of effort has been in the analysis of dislocation-particle interaction mechanisms for yielding. Less emphasis has been placed on the analysis of work hardening mechanisms in alloys containing hard particles and consequently the mathematical relationships describing this behavior are less accurate than relationships describing the yield strength. The greater emphasis on yielding mechanisms is understandable since the yield strength of an alloy is of primary concern for a structural material. However, the work hardening rate of an alloy is also of concern to a designer, since a high work hardening rate gives the designer a certain measure of safety. Also, in the field of fracture mechanics it might be possible to determine the plastic energy dissipated at the tip of a moving crack with the knowledge of stress state as a function of position and the work hardening as a function of stress. In metallic systems the plastic energy as well as the surface energy control the fracture process.

The objective of this study was to utilize existing dislocation-particle interaction theories, which were developed to predict the flow properties of single crystals containing hard particles, to analyze

the flow properties of polycrystalline α-iron with a dispersion of hard spherical particles. Conclusions about the correctness of a particular model can only be made from tests of single crystals. The emphasis in this study was to use relationships based on measureable material variables, such as particle diameter and spacing, volume fraction of second phase, matrix Burgers vector and shear modulus and grain size, to calculate the flow properties of two phase polycrystalline alloys.

Two phase alloys containing a dispersion of hard particles may be produced in the three following ways: 1) nucleation and growth 2) internal oxidation 3) powder metallurgical techniques. A random dispersion of the second phase can obtained with all three techniques although a complex grain boundary structure may result from the nucleation and growth process in polycrystalline material. The boundary region may have a heavy grain boundary network of the second phase with a precipitate free zone adjacent to the network. A grain boundary structure such as this would alter the yield and flow behavior of an alloy when compared to an alloy without this grain boundary structure. The second phase in the alloys investigated was formed by a nucleation and growth process which resulted in a complex grain boundary structure as mentioned previously. This problem was overcome by the use of an allotropic phase change, after the aging treatment, which refined the grain structure and spheroidized the grain boundary network. The final structure was a random dispersion of particles in a soft polycrystalline matrix with the grain boundary network spheroidized and no longer positioned at a grain boundary.

II. EXPERIMENTAL TECHNIQUES

A. Alloy Production and Heat Treatment

Alloys with the volume fractions listed in Table I were cast from 99.95% purity electrolytic iron (Glidden A-104) and 99.9% initial purity tantalum rod. The tantalum rod was given a three pass zone refining treatment prior to use. The composition of the iron and tantalum, prior to zone refining, is given in Table II. An induction furnace was used for preparing the ingots with the iron and tantalum held at 1750°C under argon for 30 minutes prior to pouring.

The ingots were form rolled at 1000°C from 1.25 in. diameter down to 0.50 in. square rods. The tensile specimens, which were machined from the square rods, were encapsulated in quartz and solution treated for 1 hour at 1400°C, quenched into 45°C water and then aged in a molten salt bath for 1 hour at 700°C. The grain structure was refined and the grain boundary network spheroidized by heating the samples for 10 minutes at 1100°C. Protective stainless steel bags were used to enclose the samples during this treatment. The final grain size was achieved by controlling the cooling rate during the allotropic phase change of $\gamma \rightarrow \alpha$. The final machining step was to grind off the surface oxide and to grind a uniform cross-section. The specimens were given an anneal for 30 minutes at 800°C to relieve any surface deformation caused by the grinding operation. A schematic of the heat treating cycle is shown in Fig. 1.

B. Alloy Analysis

The crystal structure and the lattice parameters of the second phase were determined from second phase particles extracted from an Fe- 2 At. % Ta alloy which had been aged for 5 hours at 800°C.

X-ray diffraction patterns were obtained from the particles with an 11.46 cm diameter Debye-Scherrer camera and using Cr K_α radiation. The film shrinkage was accounted for by loading the film in the Straumanis position. The lattice parameters a_o, c_o, and the c/a ratio were determined by a method of successive approximations outlined by Massalski and King.[1]

The equilibrium volume fraction of second phase was determined with the aid of the electron beam microprobe analyzer and the application of the lever arm principle. The total tantalum intensity of each alloy was determined from specimens in the solution treated condition and the tantalum intensity of the second phase from a specimen aged 100 hour at 800°C. The matrix composition was determined by comparison of the lattice parameter of iron versus tantalum content in the single phase samples with the lattice parameter of the two phase alloys. The lattice parameters of the iron alloys were determined with a Norelco X-ray diffractometer using Cu K_α radiation and a crystal monochromator to reduce the flourescent iron radiation.

Particle diameter distributions were determined by measuring 200-300 particles which were extracted from the alloys with carbon films. The specimen surfaces were prepared metallographically with at least 3 etch-polish steps to insure a scratch free surface with a minimum of deformation. The surfaces were cleaned with hot soap and water, rinsed with alcohol, ultrasonically cleaned in an acetone solution, etched, swabbed with hot soap and water and finally rinsed with alcohol and dried. These steps were taken to assure a clean surface prior to depositing the carbon. The carbon was deposited in a vacuum evaporator, a grid scribed in the carbon layer and extracted

in an acetic 10% perchloric acid solution with 25 volts applied across the sample and a stainless steel cathode.

The replicas were examined in an Hitachi HU-125 electron microscope at 100 KV. The magnification was calibrated by means of a calibrated carbon grating produced by E. H. Fullam Co. The dislocation structure was evaluated by means of transmission electron microscopy using an Hitachi HU-125 electron microscope at 100 KV. Foils of the undeformed structure were obtained from slices which had been heat treated, ground to 0.010 in. and chemically thinned to 0.002-0.003 in. thickness in a solution of 85 parts H_2O_2, 10 parts H_2O and 5 parts of HF. Discs, 3 mm in diameter, were punched out and jet polished in an acetic 10% perchloric acid solution at 10 volts. Foils of the deformed structure were obtained by spark cutting a 0.015 in. slice from the reduced section of a deformed tensile specimen, with the remainder of the treatment similar to the undeformed slices.

The grain size and shape were examined metallographically using interference microscopic techniques. The randomness of the crystallographic grain orientation was determined with the X-ray Laue back reflection technique, with specimens parallel and perpendicular to the form rolling direction.

Experimental stress-strain data was obtained with 0.250 in. diameter tensile specimens with an Instron tensile testing machine at a strain rate of 3×10^{-4}/minute. The load was measured with an accuracy of ± 0.5% and a sensitivity of 1 kg. The change in length was measured directly from the chart which was synchronized with the crosshead movement. The gage length was determined by grinding the reduced section of the tensile specimens with a square fillet, and could be measured with an accuracy of 0.5%.

III. STRUCTURAL ANALYSIS OF ALLOYS

The flow characteristics of two phase alloys, with a dispersion of hard particles as the second phase, are dependent on the properties and morphology of the individual phases. Properties such as the flow stress of the two phases, matrix-particle interface properties, elastic properties of the phases and the shear modulus of the matrix are important. Morphological characteristics such as the size distribution, shape, randomness and spacing of the second phase, the matrix grain size, dislocation arrangement and randomness of the grain orientations determine the yielding and work hardening properties of two phase alloys. The above characteristics have been determined for the two phase iron alloys investigated and are discussed in the following section.

A. Phase Relations in the Fe-Ta System

Knowledge of the equilibrium phases which will be present in an alloy may be found from the equilibrium phase diagram, and for the Fe-Ta system are shown in Fig. 2. in a phase diagram proposed by Sinha and Hume-Rothery.[2] It can be seen, that there are stable α, γ and δ phase regions and that the intermetallic compound Fe_2Ta is the phase in equilibrium with these phases. The phases α and δ have the body centered cubic structure and γ the face centered cubic structure. The maximum solubility of tantalum in iron occurs in the δ phase at 1440°C and is about 2.8 at. % Ta. The δ phase decomposes eutectoidally at 1293°C by the following reaction:

$$\delta(1.1 \text{ at. \% Ta}) \rightleftharpoons \gamma(0.5 \text{ at. \% Ta}) + Fe_2Ta$$

and the γ phase decomposes peritectoidally at 974°C by the following reaction:

$$Fe_2Ta + \gamma(0.3 \text{ at. \% Ta}) \rightleftharpoons \alpha(0.6 \text{ at. \% Ta})$$

If the equilibrium phase relations are known and the compositions of the phases are known the equilibrium volume fraction of the phases may be determined from the phase diagram. Since the compositions of the phases were not known for the Fe-Ta system, analysis of these important parameters was undertaken.

The solubility of the compound Fe_2Ta in α iron at 800°C was determined because of the need to know the matrix composition for the volume fraction analysis and the contribution of tantalum to solute hardening. The composition of the matrix was determined by measuring the lattice parameters of solution treated samples of iron-tantalum alloys as well as the lattice parameter of two phase alloys. The results of this study are shown in Fig. 3 and from these results it was determined that the matrix composition of the two phase alloys was 0.1 at.% Ta. Hansen[3] has shown the Laves phase Fe_2Ta to have a stoichiometric composition with no range of stability. Goldschmidt[4] found that the Fe-Nb Laves phase had a difference in lattice parameter of $\Delta a_o = +0.021$Å and Δ c/a = -0.004 when comparing compounds with 20 and 40 at. % niobium. The lattice parameters of the Fe-Ta Laves phase in equilibrium with α iron were determined and are listed in Table III along with the results of others. Comparison of the a_o and c/a values given by Hansen and the data for the Laves phase in equilibrium with α iron showed the same deviation as Goldschmidt found for Fe_2Nb. Also, the lattice parameters from this work match closest with those listed in

the ASTM Powder Diffraction File for Fe_7Ta_3. The similarities between the Fe-Nb and Fe-Ta systems also support the conclusion that the Fe-Ta Laves phase is stable over a range of composition because the Fe-Nb Laves phase is stable over a range of 20 at. % niobium.[8]

B. Characteristics of the Fe-Ta Laves Phase

There are presently 223 known binary Laves phases of which 210 have a transition element as one element. There are five known structures which the Laves phase forms and these are the cubic $MgCu_2$ and UNi_5 structures and the hexagonal $MgZn_2$, $MgNi_2$ and $CaCu_5$ structures. The hexagonal $MgZn_2$ structure, of primary interest in this study, has hexagonal symmetry with an abab stacking sequence and 8 zinc atoms and 4 magnesium atoms per unit cell. It has been found by Dwight[9] that the Laves phase will form from atoms with Goldschmidt radius ratios ranging from 1.05 to 1.68 with the atoms expanding or contracting to satisfy the radius ratio of 1.225 in the compound. Although the atom sizes strongly effect whether the Laves phase is stable they have little effect on which crystal structure will be formed. Electronic contributions appear to have a controlling effect on which crystal structure will form; however, a quantitative correlation is not yet possible.

The Fe-Ta Laves phase has been identified by x-ray diffraction as isomorphous with the hexagonal $MgZn_2$ type structure (C14). The lattice spacings and intensities are listed in Table IV along with the data for Fe_7Ta_3 listed in the ASTM Powder Diffraction File. Because of the close match of the interplanar spacings and intensities with that of Fe_7Ta_3, it is thought the Fe-Ta Laves phase in equilibrium with α iron is close to this composition. Whether the non-stoichiometric

composition is the result of iron atoms substituted for tantalum atoms or from vacant tantalum sites is not known. However, in the compound $MgZn_2$ it was found[10] that vacancies accounted for the non-stoichiometric composition.

The ductility of the Fe-Ta Laves phase has been studied by G. Sasaki[11] by observing the region around a vickers microhardness indentation made in single phase samples of the compound Fe_2Ta. The indentations made at room temperature resulted in short cracks at the corners of the indentation and some evidence of plastic flow. The measured hardness was 1000 kg/mm^2.

C. Structural Analysis of Two Phase Alloys

1. Alloy History

An understanding of the structural characteristics of the two phase alloys used in this study requires an examination of the alloys during each stage of processing. The homogeneity of any two phase structure is dependent upon the segregation which occurs during solidification. The slow diffusion rate of tantalum in iron would require a very high temperature for homogenizing, therefore small diameter ingots were used to minimize segregation during solidification. This approach worked very well as no segregation could be detected in the cast alloys. After casting, the ingots were hot worked to a 0.50 in. by 0.50 in. shape at 1000°C. This hot working temperature was chosen to reduce texturing from the deformation process. High purity iron heated to 1000°C would oxidize internally in a very short time; however, the Fe-Ta alloys had little difference in oxide morphology between the cast and hot worked structure.

The second phase was formed, after solution treating at 1400°C and quenching to room temperature, by the following reaction:

$$\alpha(\text{supersat.}) \rightleftharpoons \alpha + Fe_2Ta$$

at 700°C. The Fe_2Ta particles which formed during this reaction were plate shaped and there was a heavy network of the Laves phase at the grain boundaries, as shown in Fig. 4a. The final treatment was to heat the alloys to 1100°C, as shown in Fig. 1, at which the stable structure is $\gamma + Fe_2Ta$. The effect of this treatment was to spheroidize the matrix and grain boundary particles, and refine the grain size. The effect of this treatment on the grain boundary and matrix particles can be seen by comparing Fig. 4a and Fig. 4b. Also, after the allotropic phase changes of $\alpha \rightarrow \gamma \rightarrow \alpha$ the prior grain boundary network is positioned within the grains rather than at the boundaries.

2. Second Phase Morphology

The morphology of the second phase has been characterized by determining the diameter distribution, mean particle diameter and standard deviation, volume fraction, interparticle spacing and the spatial randomness of the particles. The particle diameter and spatial randomness were measured from extraction replicas by a method outlined by Ashby and Ebeling.[12] There are many techniques for measuring the average particle diameter such as electron transmission microscopy of thin foils, optical microscopy, point counting, small angle x-ray diffraction, and extraction replicas. Since the spread of the particle diameter about its mode is required to evaluate the interparticle spacing, point counting techniques and small angle

x-ray diffraction techniques are not suitable. Also, the particle diameters in the two phase alloys were too small to be measured at magnifications obtainable with the optical microscope. Extraction replicas were chosen because of their ease of preparation, freedom to examine large areas at low magnification and because the particle sizes were close to the foil thickness required for transmission of electrons through an iron foil. This condition would not yield a volume distribution but a planar distribution as do extraction replicas. Also, comparison of the diameter distribution of SiO_2 particles in copper were measured with thin foils and extraction replicas by Ashby[12] with very close agreement between the two techniques. One precaution that must be taken with extraction replicas is to be sure all particle diameters are extracted with equal probability. For chemically inert particles in the size range of 100Å to 10,000Å extraction is equally probable and since the Laves phase particles in iron are within these limitations the extraction technique was selected as the best method for particle sizing. Typical particle dispersions of the alloys investigated are shown in Fig. 5, also optical micrographs of the alloys are shown in Fig. 6.

The particle diameters of two to three hundred particles were measured for each alloy, the number of particles with diameters in groups of 250Å determined and the cumulative probability plotted versus the diameter. Alloys 2,3,4, and 5 approximated to normal distributions and alloys 6 and 7 to log normal distributions as shown in Fig. 7. The arithmetic mean is given by the 50% point and the arithmetic standard deviation by the difference between the 50 and 84% points of the normal distribution and the geometric mean and geometric

standard deviation by the same points of the log normal distribution. The mean and standard deviation for the six alloys studied are listed in Table I. The geometric means and geometric standard deviations were converted to arithmetic means and arithmetic standard deviations.

The variation of the extraction factor from replica to replica makes the extraction technique unsuitable for volume fraction determinations. The volume fraction of second phase could not be determined from the phase diagram because the composition of the Laves phase in equilibrium with α iron was not known. Therefore, the volume fractions of Laves phase present in the alloys investigated were measured with the aid of an electron beam microprobe analyzer. This technique, proposed by Waldman et al.,[13] makes use of the lever arm principle; with the boundary conditions evaluated with the electron beam microprobe analyzer. Using the intensities measured with the microprobe, the volume fraction of Laves phase in equilibrium with α iron is given by the following relationship:

$$f = I - I_A / I_B - I_A$$

where I is the total intensity of tantalum in the alloy, I_A the intensity of tantalum in α iron in equilibrium with the Laves phase and I_B is the intensity of tantalum from the Laves phase in equilibrium with α iron. The intensities were corrected for background from the iron. The total intensity was measured from specimens in the solid solution condition, and the intensity from the Laves phase was obtained from an overaged specimen. The intensity of tantalum in α iron was determined with the aid of x-ray diffraction and the electron beam

microprobe analyzer. The lattice parameters of solution treated and two phase samples were examined with the results shown in Fig. 3. The matrix composition was constant for all alloys in the spheroidized condition and this composition was found to be 0.1 at.% Ta. The matrix composition was converted to tantalum intensity from the intensity versus composition data obtained from the solid solution samples. The volume fractions of the six alloys studied are listed in Table I.

The interparticle spacing of the particles on a random plane can be calculated from the following relationship:[12]

$$\lambda = 0.5 \left\{ \frac{\pi}{6f} \left(1 + \frac{\sigma^2}{\bar{D}^2} \right) \right\}^{1/2} \bar{D}$$

where f is the volume fraction of Laves phase, $\bar{D}$ is the average particle diameter and σ^2 is the standard deviation. The center to center spacing as well as the between particle spacing ($\lambda - \bar{D}$) are listed in Table I.

The spatial randomness of the Laves phase in the iron matrix was investigated because of the complex heat treatment required to achieve the desired morphology. The randomness was examined by dividing the extraction replica micrographs into squares and counting the number of particles in each square. The probability that a square contained r particles, P(r), was plotted versus the number of particles, r, to obtain the distribution curve. The experimental distribution was compared with the Poisson distribution where:

$$P(r) = \mu^r / r!\ \exp(-\mu)$$

where P(r) is the probability that a square contains r = 0,1,2,3,. . . particles and μ is the average number of particles. The comparison between the Poisson distributions and the experimentally determined distributions are shown in Fig. 8. It was concluded that the Laves phase particles were randomly distributed in the iron matrix because the Poisson distribution was derived from the assumption of complete randomness and the experimental distributions match the Poisson distribution. The area of the squares was decreased for samples with increasing particle density to keep the average number of particles per square close to 1.

3. Matrix Characteristics

The interparticle spacing, diameter and volume fraction of the second phase are necessary variables to determine for the calculation of the flow properties of a two phase system, but the dislocation structure, matrix flow properties, sub grain size and grain size are also necessary structural features to evaluate.

The randomness of the grains was examined by the back reflection Laue technique. Directions parallel and perpendicular to the tensile axis were examined for each alloy. It was concluded that little texturing had occurred during the forming process or subsequent heat treatments. A typical Laue back reflection photograph obtained for both perpendicular and parallel directions is shown in Fig. 9.

The grain boundaries of the spheroidized structure were difficult to reveal with an optical microscope because the second phase particles were large enough to obscure the boundaries. The grain structure of alloys 2 and 5 are shown in Fig. 10 and comparison with an ASTM grain size chart shows the grains to be about 3-5. The grains had a large

variation in size within a given sample and in alloys with lower volume fractions the grains were equiaxed while in the alloys with a higher volume fraction the boundaries became more irregular. This effect is consistent with observations of grain shape in recrystallized two phase alloys.[14]

Following the $\alpha \rightarrow \gamma \rightarrow \alpha$ treatment and an anneal at 800°C, the alloys had a sub grain structure which was dependent on the particle spacing. The substructures of alloys 2,4 and 6 are shown in Fig. 11 and Fig. 12. Electron diffraction analysis was used to verify that the structure observed in these alloys were sub grains and the results of one of these studies is shown in Fig. 11. As can be seen, the patterns from the two sub grains are nearly identical as expected from material with a low angle boundary between them. The lack of texturing in these alloys rules out the possibility that these are high angle boundaries of a highly textured material. Also, any texture in this material would be a rod texture, because of forming conditions, and the grains would have a random orientation around the foil normal which was also the rod axis. The sub-grain size of alloys 2 and 6 have been determined by lineal analysis, and the sub-grain size of alloy 2 was 3200Å and alloy 6 was 2000Å.

Studies of deformed samples were conducted to determine whether the second phase fractured during plastic deformation or whether the particle/matrix interface had failed. After plastic strains of 10-20%, approximately the ultimate strain, neither fractured particles nor failed interfaces were observed. The dislocations were arranged in tangles around the particles as shown in Fig. 13 for alloys 2 and 4. The tangles around the particles are very similar to the secondary

dislocations proposed by Ashby[15] in his theory on the work hardening of two phase materials. No evidence of dislocations loops, as proposed by Fisher, Hart and Pry,[16] were observed.

IV. DISCUSSION OF DISLOCATION-PARTICLE INTERACTION MECHANISMS

A. Yielding Mechanisms

The interaction between a dislocation and a hard incoherent spherical particle embedded in a soft matrix is the only dislocation-particle interaction mechanism which needs to be considered because the Laves phase in iron fits this category. The yielding behavior of alloys with this type of structure have been thoroughly investigated for both single and polycrystalline material, with the first mathematical relationship describing the yield stress as a function of particle spacing proposed by Orowan.[17] He proposed that a critical stress was reached at which a dislocation expanded to a semi-circular loop between the particles, where the particles acted as obstructions to dislocation movement in the slip plane. The flow stress is given by the sum of the stress required to move the dislocation through the matrix unobstructed by particles and the stress required to bypass the particles. The following relationship would then describe the flow stress:

$$\tau = \tau_o + \frac{2T}{b\lambda} \qquad (1)$$

where τ is the critical resolved shear stress of the two phase material, τ_o the critical resolved shear stress of the matrix, T is the line tension of the dislocation, b is the Burgers vector and λ is the mean planar interparticle spacing. In the simplest case the line tension can be taken as $Gb^2/2$ per length resulting in the following relationship:

$$\tau = \tau_o + \frac{Gb}{\lambda}$$

where G is the shear modulus. Nabarro[18] has evaluated the line tension of a dislocation and substituting this result into Eq. (1) results in the following:

$$\tau = \tau_o + \frac{Gb\phi}{2\pi(\lambda-\bar{D})} \ln\left(\frac{\lambda-\bar{D}}{2b}\right) \qquad (2)$$

$$\phi = \frac{1}{2}\left(1 + 1/1 - \nu\right)$$

where $\bar{D}$ is the mean particle diameter. The term $(\lambda - \bar{D})$ was introduced to account for the finite particle size.

Further refinements have been made on the Orowan theory by Ashby[19] where he evaluated the critical configuration for bypass and the variation of the line tension with dislocation character. The approach used by Ashby was to determine the force exerted on a particle by a bowing dislocation, where the force is a function of the angle between the dislocation segments on either side of the particle. The force on a particle is then given by:

$$F = 2E(\theta)\,\mathrm{Cos}\,\theta$$

$$E(\theta) = \frac{Gb^2}{4\pi} \ln\left\{\frac{\bar{D}}{r_o}\left[1 + \left(\frac{\lambda}{\bar{D}} - 1\right)\mathrm{Sin}\,\theta\right]\right\}$$

where θ is the angle between adjacent dislocation segments bowing around a particle. For an edge dislocation the critical stress is:

$$\tau_e = \frac{Gb}{2\pi\lambda} \cos\theta \ln\left\{\frac{\bar{D}}{r_o}\left[1 + \left(\frac{\lambda}{\bar{D}} - 1\right)\sin\theta\right]\right\} \qquad (3)$$

Ashby found the critical configuration occurred when $\theta = 0°$ to $30°$ but was always greater than $0°$. The critical angle θ decreases with increasing particle spacing and increasing (D/λ).

Besides acting as a simple obstacle to slip, a second phase particle can cause stresses in the matrix which impede dislocation motion. The difference in the coefficient of thermal expansion of the matrix and the particle can result in long range matrix stresses of the order of $2G\delta f$, where G is the matrix shear modulus, δ is the misfit and f is the volume fraction of particles. Also, differences in elastic modulus result in image forces which can attract or repel a dislocation. The long range back stress due to this difference is approximately:

$$\tau = \Delta G b f / 4\pi\lambda \qquad (4)$$

In most cases where the bypass stress is large the effect of differences in coefficient of thermal expansion and elastic modulii is small and may be neglected.

The randomness of the particle spacing will affect the sharpness of the measured flow stress. It was found by Kocks[20] that if the critical bypass configuration is $\theta = 0°$ then the macroscopic flow stress of the random array of particles is 0.85 times the average local Orowan stress.

The Orowan relationship has been tested with a large number of alloy system and both the simple and more sophisticated relationships satisfactorily fit the results. Tests with copper single crystals with SiO_2 particles and BeO particles have been conducted by Ebeling

and Ashby[21] and Jones and Kelly,[22] respectively. Their data fit, with reasonable accuracy, Eq. (4) with $\theta = 0°$. Aluminum-copper single crystals have been tested by Dew-Huges and Robertson[23] and the critical resolved shear stress was shown to vary linearly with λ^{-1}. The slope of this plot differed from the theoretical value and there was a great deal of scatter, however a somewhat better fit was obtained when Kelly and Nicholson[24] replotted their data according to Eq. (2).

The application of the Orowan relationship to the prediction of the flow stress of an alloy must be done with care. The structural features of the alloy must fit the model for which the Orowan relationship was derived. The particles must be non-shearing, the matrix must be in the annealed state, the particles must be dispersed within the grains and not concentrated at boundaries and solid solution strengthening and strain aging must be taken into account in BCC systems. Also, when analyzing polycrystalline materials the randomness of the grain orientations and the grain size must be known.

B. Work Hardening Mechanisms

The first model proposed for the work hardening of single crystals containing a hard second phase was by Fisher, Hart and Pry[16] and it was based on an increased bypass stress necessary because of circular loops which are left at each particle as the dislocation bypasses that particle. The model assumes that no cross-slip occurs and that these loops remain in the primary slip plane and exert a shear stress in the matrix which opposes further dislocation motion. The results of this model state that the flow stress depends on the volume fraction and the radius of intersection of the particle with the glide plane. The following relationship was proposed:

$$\Delta\tau_h = \frac{cf^{3/2}NGb}{r} \qquad (5)$$

$$\Delta\tau_h = (\tau - \tau_y)_{\text{particles}} - (\tau - \tau_y)_{\text{without particles}}$$

where c is a constant equal to about 3, f is the volume fraction, N is the number of concentric loops around the particle, G is the matrix shear modulus, b is the Burgers vector and r is the radius of intersection of the particle with the glide plane. Fisher et al.,[16] also proposed that the increment in flow stress, $\Delta\tau_h$, would reach a maximum because the stress build-up around the particle would ultimately fracture the particle. This maximum stress was given as:

$$\Delta\tau_h = 3f^{3/2}\tau_c$$

Concentric dislocation loops have never been observed in plastically deformed alloys containing hard particles, while it has been found by Dew-Hughes et al.,[23] that Al-Cu single crystals oriented for single slip instead slipped on many intersecting slip systems. Ebeling and Ashby[21] found that copper single crystals with up to 1 vol. % of SiO_2 deformed by single slip when oriented for single slip, but that the stage I region of the stress-strain curve was replaced by an approximately parabolic stage. The greater volume fraction of second phase in the Al-Cu alloys is thought to account for the more turbulent flow in these crystals when compared to the copper crystals.

The second work hardening model was proposed by Ashby[15] and he proposed the following relationship:

$$\tau = \tau_y + CG(bf\gamma/\bar{D})^{1/2} \qquad (6)$$

where τ is the shear stress required to flow the two phase alloy, τ_y is the critical resolved shear stress of the two phase alloy, C is a constant equal to 0.2 to 0.4, γ is the shear strain, b the Burgers vector, f the volume fraction, and $\bar{D}$ is the mean particle diameter. This relationship was found to fit the work hardening data of Ebeling et al.,[21]. It was observed that with increasing volume fraction single crystals oriented for single slip deformed more homogeneously with unobserveable slip lines, Laue patterns blurred and formed Debye rings and finally shape changes became more typical of a polycrystal than a single crystal. The observation of dislocation networks around the particles accompanied these changes in slip behavior. In the proposed model Ashby stated that secondary dislocations are nucleated at the particle-matrix interface to relieve the stresses from the dislocation loops on the primary slip plane. The work hardening occurs because of the interaction between primary and secondary dislocations. Ashby assumed that the number of loops intersecting per unit of area of slip plane was,

$$N_L = 3\gamma f/\pi b\bar{D} \qquad (7)$$

and that the flow stress was related to the dislocation density by the force exerted by a dislocation loop (secondary dislocation) opposing a straight dislocation (primary dislocation) which is 0.25 Gb^2 and the average number of loops per length of dislocation which is $(N_L)^{1/2}$. The total force opposing a straight dislocation is 0.25 Gb^2 $(N_L)^{1/2}$. The force due to the stress increment above the

initial yield stress, $(\tau - \tau_o)b$, is equated to the force and the result is the final expression, Eq. (6).

C. Relationship Between Single Crystal Deformation and Polycrystal Deformation

The previous expressions which related stress to strain and to particle morphology have been based on shear stress and shear strain because of the need to evaluate the dislocation motion on a given slip plane. There are very few applications of single crystals to engineering use, so if these models of particle/dislocation interaction are to be applied to engineering materials they must be related to polycrystalline deformation. The applied tensile stress can be resolved onto a given plane and in a given direction through geometric considerations with the following relationship:

$$\sigma = M\tau = \tau/\sin\chi\cos\lambda \qquad (8)$$

where σ is the applied tensile stress, τ is the shear stress on a given plane in a given direction, χ is the angle between the slip plane and tensile axis, λ is the angle between the slip direction and the tensile axis and M is the Schmid factor.

A polycrystal is a set of single crystals each oriented randomly with respect to the tensile axis, each with a different Schmid factor. There have been two attempts to calculate a Schmid factor for polycrystalline materials and the first of these attempts was by Sachs.[25] He determined the average orientation factor for all twelve slip systems in an FCC crystal assuming that each grain deformed independently of its neighbors. Sachs found a Schmid factor of 2.238. Sachs analysis requires a series of parallel but free single crystals

with an equal tensile strain, and unequal strains in other directions and unequal tensile stresses in each grain. This approach gives a lower limit to the polycrystalline stress strain curve.

The second approach, to determine a Schmid factor for polycrystals, was presented by Taylor[26,27] where he considered the minimum work required for shear on five systems which satisfied the continuity conditions at a grain boundary. Taylor equated the energy expended during a small strain of unit volume of a grain on either side of the boundary to the work done by the external stress as follows:

$$\sigma d\varepsilon = \sum_{i=1}^{n} \tau_i d\gamma_i \qquad (9)$$

Assuming τ_i is the same on all systems then,

$$\frac{\sigma}{\tau} = \frac{\sum_{i=1}^{n} d\gamma_i}{d\varepsilon} = M$$

By finding the set of slip systems in an FCC system which satisfied the continuity conditions yet minimized the value of $\sum_{i=1}^{n} d\gamma_i$ Taylor found the set of systems most likely to deform. He found ninety six sets of systems which would fit these criteria and evaluating forty four systems he calculated an average M of 3.06.

Body centered cubic crystals deform by pencil glide where the slip direction is crystallographic but the slip plane is that of maximum resolved shear stress containing the crystallographic direction. In reality slip is confined to definite planes, but in a BCC crystal there are enough planes on which slip will occur that contain the ⟨111⟩ directions to make deformation approximately non-planar. In

iron both the (110) and the (112) planes have been observed as slip planes; both contain the ⟨111⟩ direction. The Taylor factor, M, has been calculated for pencil glide by Hutchinson[28] and Chin and Mammel[29] and they found that M was equal to 2.75. Keh[30] used this value for the Taylor factor to calculate the shear stress-shear strain curve of polycrystalline iron and found that the calculated curve fell between the single crystal curves for crystals oriented in the [100] and [111] directions.

Using the Taylor factor, M, the single crystal relationships, Eqs. (3) and (6), can be converted to polycrystalline tensile stress-strain relationships as follows:

$$\sigma_y = \sigma_o + \frac{MGb}{2\pi(\lambda-\bar{D})} \ln\left(\frac{\bar{D}}{4b}\right) \qquad (3a)$$

assuming $\theta = 0^\circ$ and setting σ_o equal to the matrix flow strength.

$$\sigma = \sigma_y + m^{3/2} CG \left(\frac{bf\varepsilon}{\bar{D}}\right)^{1/2} \qquad (6a)$$

V. RESULTS OF STRESS-STRAIN PREDICTIONS

The calculation of polycrystalline stress-strain behavior of single phase material from single crystal stress-strain curves has been achieved with reasonable accuracy for both FCC and BCC crystals. However, the prediction of polycrystalline stress-strain behavior from models of dislocation interactions, in single phase material, and particle-dislocation interactions, in two phase material, has received little attention. In this study, it has been found that up to some limiting strain the stress-strain behavior of a two phase alloy has been predicted from a relationship based on particle-dislocation interactions.

The yield strengths of the alloys investigated were calculated with Eq.(3), assuming $\theta = 0^\circ$, and the results have been compared to both the proportional limit and the 0.2% offset yield strength in Table V. The 0.2% offset yield strength of alloys 2,3,4 and 5 compare very well with the calculated values, but the results of alloys 6 and 7 do not match so well. In Eq. (3a) the matrix yield strength, σ_o, was taken as 5.5 kg/mm^2. This value was determined from polycrystalline iron samples (Alloy 1) heat treated and tested similarly to the two phase alloys. In Eq. (3a) the Burgers vector was taken as 2.48Å the shear modulus G as 8.47×10^3 kg/mm^2 and the cut off radius, r_o, as 4b. Agreement between the slope of Eq. (3a), $0.85\ MGb\phi/2\pi$, and the slope obtained from a plot of the 0.2% yield strength versus $\ln (d/4b)/(\lambda-\bar{D})$ was within 15%. The experimental curve is presented in Fig. 14 and the values of the calculated and experimentally determined slopes are listed in Table V. Data from alloys 6 and 7 were not used for the determination of the experimental slope.

The flow curves of the two phase iron alloys tested were parabolic up to about 5% plastic strain. A linear relationship was obtained when σ_h, the difference between the flow stress and the yield stress of the two phase alloys, was plotted versus the square root of the true plastic strain. The results of this evaluation are shown in Fig. 15 and the deviation from the linear relationship marked a change in the work hardening mechanism. The strain at which the data deviated from linearity decreased with decreasing $(\lambda-\bar{D})$; however, the decrease was only slight. The slopes obtained from Fig. 15 compared very well with the slopes of Eq. (6a), $M^{3/2}CG(bf/\bar{D})^{1/2}$, when C was set equal to 0.46. The experimentally determined slopes and calculated slopes are listed in Table VI, as is the slope obtained from a plot of σ_h versus $(bf\varepsilon/\bar{D})^{1/2}$. A linear relationship was also obtained when σ_h was plotted versus $(bf\varepsilon/\bar{D})^{1/2}$, as shown in Fig. 16.

The value $\Delta\sigma_h$, which equals σ_h(particles) minus σ_h(no particles), has been plotted versus the true plastic strain in Fig. 17. The results show that the work hardening contributed by the particles saturates at about 5% plastic strain. This value is very nearly the same as the strain at which the σ_h versus $\varepsilon^{1/2}$ data deviates from a linear relationship.

Using Eq. (6a), the flow properties of these alloys have been calculated as a function of strain and the results of these calculations are shown in Fig. 18 and Fig. 19. These curves were calculated using the experimentally determined value of the proportional limit for σ_y as this was the smallest strain at which plastic flow was detected. Up to about 3% plastic strain the calculated and experimental flow curves showed remarkably good agreement. Above 3% plastic strain the deviation

increased with the volume fraction of second phase. Even with this disagreement, the calculated values and experimental values of the ultimate stress were within 15% to 35%, depending on volume fraction of second phase.

VI. DISCUSSION OF RESULTS

A. Yielding Behavior

The applicability of the Orowan relationship to predict the yield stress of an alloy with a dispersion of a hard second phase has been well established. However, care must be taken when applying this relationship to alloys with a complex thermal or thermal-mechanical history because the model is based on particle-dislocation interactions only and not on dislocation-dislocation interactions. The contribution to the yield strength from the matrix dislocation density must be evaluated separately from the contribution from the particles. The alloys investigated had a complex thermal history which resulted in a high dislocation density but these dislocations were arranged into sub grain boundaries by an annealing heat treatment. Also, the matrix strength was determined with samples which had undergone the same complex thermal treatment as the alloys but without particles.

The matrix flow stress was measured with uniaxial tensile samples of iron which had been treated similarly to the alloys. The iron used for these samples was the same as that used for the alloys and were tested at the same temperature and strain rate as the alloys. A yield point was observed in the iron tensile samples which was never observed in the alloys. In the Fe-Ta alloys the carbon was probably removed from solution by the tantalum, which is a strong carbide former. The yield stress of titanium gettered polycrystalline iron tested at 300°K was found to be 4.8 kg/mm^2 by Cuddy and Leslie.[31] Their samples had an ASTM grain size of 4-5 while the iron samples tested in this study had a grain size of 1-2. The combination of a larger grain size, which would lower the yield stress, and the presence of interstitial carbon, which would

raise the yield stress, resulted, fortuitously, in a yield strength similar to that found by Cuddy and Leslie. Since the Fe-Ta alloys had a grain size of 3-5 and were probably free of interstitial carbon, the yield stress of 5.5 kg/mm^2 observed for the iron samples was taken as the matrix flow stress of the two phase alloys at 20°C. Also, the contribution of 0.1 at. % Ta to the solute hardening was about 1%, therefore it was neglected.

The yielding behavior of alloys 2,3,4 and 5 obeyed an Orowan type relationship. Since the sub-grain size was dependent on the interparticle spacing in these alloys, the dependence of the yield strength on interparticle spacing could be a measure of sub-boundary dislocations pinned by the particles which subsequently bowed out from the particles. Whether the dislocations are randomly arranged in the matrix or arranged in sub-grain boundaries pinned by the particles the Orowan mechanism controls yielding, although a sub-grain size smaller than the interparticle spacing would increase the yield strength above that expected for a given interparticle spacing. The sub-grain size was smaller than the interparticle spacing in alloy 2 and larger than the interparticle spacing in alloy 6. Even though the sub-grain size was smaller than the interparticle spacing in some of the alloys an Orowan type yielding mechanism prevailed. The proportional limit of the alloys were smaller than the yield strength predicted by Eq. (3a) and was probably a measure of the movement of unpinned dislocations within the sub-grains or within the precipitate free zone, PFZ, near the original α boundary. The deviation of the yield strengths of alloys 6 and 7 from those calculated by Eq.(3a) is thought to be the result of a wide PFZ in these alloys. Also, the occurrence of quench cracks

in these alloys were observed and although precautions were taken to prevent them, cracking may have persisted. When cracking was observed the cracks were large enough to affect the load carrying area.

B. Work Hardening Characteristics

It has been found that the work hardening characteristics of polycrystalline two phase iron alloys obeyed a work hardening mechanism as proposed by Ashby and stated in Eq. (6). It was evident that the work hardening did not obey the Fisher, Hart and Pry model because attempts to fit $\Delta\sigma_h$ to $f^{3/2}/r$ resulted in a nonlinear relationship at all strains and a plot of $\Delta\sigma_h$ max versus $f^{3/2}$ also was non-linear. Also, it was quite evident from the stress-strain curves that the flow stress was not linearly dependent on strain as would be necessary with the Fisher, Hart, and Pry model. Therefore it was concluded that this model did not explain the work hardening in the alloys studied.

The occurrence of a maximum in $\Delta\sigma_h$ was the only aspect of the work hardening which coincided with the Fisher, Hart and Pry model. The FHP model predicts that $\Delta\sigma_h$ has a maximum, $\frac{d\Delta\sigma_h}{d\varepsilon} = 0$, at which the work hardening in the two phase structure equals the single phase work hardening. A satisfactory explanation for this maximum has not been proposed, although Fisher et al., claim that the particles fracture and a steady state number of loops exist around the particle. The number of loops which are predicted to exist around the particles at this maximum are 30 to 100. It is not likely that a hard particle such as an oxide or intermetallic compound would fracture under these conditions, and this has been verified by Ashby,[15] Dew-Hughes et.al.,[23] and in this study. The alloys investigated had a maximum in $\Delta\sigma_h$ at 5%

plastic strain, except alloy 7 which had a maximum at 8%, a behavior which has been observed by others.[33,34] The magnitude of $\Delta\sigma_h$ max did depend on particle morphology, as shown in Table VI, but a plot of $\Delta\sigma_h$ max versus $f^{3/2}$ was non-linear. If τ_c were a constant, and if work hardening obeyed the Fisher, Hart and Pry model then a linear dependence should have been observed. Some dependence of $\Delta\sigma_h$ max on the particle morphology is expected but at the present time a relationship other than that proposed by Fisher, Hart and Pry has not been presented.

The flow stress of a single phase material has been shown[35,36] to be a function of $\rho^{1/2}$, where ρ is the dislocation density. Also, it has been shown by Conrad[37] that ρ is inversely proportional to the grain size and that as a function of strain the flow stress is given by:

$$\sigma = \sigma_o + \alpha\mu b\beta^{1/2}\varepsilon^{1/2} \qquad (10)$$

where α and β are constants, ε is the true plastic strain, b is the Burgers vector, and μ is the shear modulus. The single phase samples tested (Alloy 1) obeyed this relationship to strains of about 5.5%. Also, the plots of $\Delta\sigma_h$ versus ε had a parabolic shape as predicted by the difference of Eqs. (10) and (6a). The deviation of a single phase material from the parabolic flow stress relationship occurred because of a change in dislocation interaction mechanism, and with the addition of hard particles to the material the strain at which this change in work hardening occurred was reduced. However, this was not shown conclusively in the Fe-Ta alloys investigated because of the small change in the strain at which parabolic hardening ceased.

The work hardening model presented by Ashby was not quite as simple as the FHP model although it is based on primary slip occurring on a single slip plane. It has been noted that the experimental work hardening data agreed with the Ashby work hardening model with fair accuracy up to some limiting strain. The deviation of σ_h from a linear relationship, as noted in Fig. 15, occurred at nearly the same strain that $\Delta\sigma_h$ reached a maximum. Also, in both limiting cases the strain was nearly independent of the particle volume fraction, spacing and diameter. It is concluded that the work hardening saturation contributed to the deviation from parabolic hardening observed in these alloys.

The slopes obtained from plots of σ_h versus $\varepsilon^{1/2}$ were found to correlate very closely with those obtained from Ashby's relationship when C was taken equal to 0.46. Ashby found that in copper single crystals containing SiO_2 particles C equaled 0.24, and that theoretically C was 0.20 to 0.40. The large value of C found in two phase iron alloys may have resulted from primary slip occurring on more than one slip plane. Ashby assumed that primary slip occurred on a single plane and that secondary slip occurred on other planes. In the two phase polycrystalline samples tested in this study primary slip was not restricted to a single slip plane.

A plot of σ_h versus $(bf\varepsilon/\bar{D})^{1/2}$ had a slope of 12.5×10^3 kg/mm^2 while the calculated slope was 17.8×10^3 kg/mm^2. The calculated slope is somewhat larger than the experimentally determined value, but the data had a large amount of scatter so that the slopes obtained from plots of σ_h versus $\varepsilon^{1/2}$ were more accurate.

C. Prediction of Flow Behavior

The calculated and experimental flow curves have been divided into two segments, small strains up to 3% plastic strain, and large strains, up to the ultimate strain. This division helped the comparison between experimentally determined flow curves and calculated flow curves at strains where the Ashby work hardening model was valid. As seen in Fig. 18, the fit between calculated and experimental flow curves was excellent and with alloys 2,3,4, and 5 the calculated yield strength could have been used and the fit would have been just as good. In all cases the shapes of the calculated curves were very similar to the experimentally determined curves.

At large strains the calculated curves were well above the experimental curves. This deviation is related to the deviation observed in the plots of σ_h versus $\varepsilon^{1/2}$, which is thought to be related to the saturation of the work hardening of the two phase alloys. Also, the conversion of single crystal data to polycrystalline with the Taylor model caused some error at strains greater than 5%. A deviation between single crystal data and calculated polycrystal data has been observed for copper single crystals oriented near the [111].[38] The results of this calculation are shown in Fig. 20 and it can be seen that the deviation in the two curves occurs at tensile strains of about 5%.

The development of a relationship to predict the flow behavior at strains greater than about 5% requires the evaluation of the mechanisms which control the work hardening saturation. Also, it is possible the Taylor factor is a function of strain because of lattice rotations which occur during plastic deformation. Even with the

deviation mentioned the error between the calculated and experimental ultimate stress varied only 15% to 35%, depending on alloy, as shown in Table VI.

VII. CONCLUSIONS

The use of relationships based on particle-dislocation interaction mechanisms to predict the flow properties of polycrystalline α-iron containing hard spherical particles has been undertaken in this study. Both the yield stress and the stress-strain behavior of these two phase iron alloys have been measured and compared with calculated values with good agreement.

The yield strength values depended on the interparticle spacing in a manner similar to that proposed by Orowan, but the best fit was obtained with an Orowan type relationship as modified by Ashby.[19] This relationship accounts for the dependence of the line tension with dislocation character and the critical configuration for dislocation by-pass.

The work hardening characteristics of the two phase iron alloys depended on the particle diameter, volume fraction of second phase and the strain in a manner proposed by Ashby.[15] Ashby proposed that the flow stress had a parabolic relationship to the strain and up to a limiting strain this relationship was obeyed by the iron alloys tested. At this limiting strain the increase of the flow stress of the two phase structure over that of the single phase structure reached a maximum and it was concluded that this saturation of the particle hardening was responsible for the deviation of the flow stress from the parabolic relationship. The slopes obtained from plots of the flow stress versus the square root of the strain compared very well with the slopes predicted by Ashby's work hardening model.

The flow curves of the alloys were calculated using Ashby's work hardening model and excellent comparison was found for all the alloys

up to 3% plastic strain. Both the magnitude and the shape of the calculated curves matched the experimentally determined data. Above 3% strain, the calculated data was greater than the experimental data with the deviation increasing with increasing volume fraction. The difference between the calculated and experimentally determined data was caused by the saturation of particle contributed work hardening and by the conversion of the flow relationship from that of single crystal deformation to polycrystalline deformation. The difference between the experimentally determined and the calculated ultimate stress was 15% to 35% depending on the volume fraction of second phase.

It was concluded that the flow stress of a two phase polycrystalline alloy, with hard particles as the second phase, can be successfully predicted from a relationship which depends on the morphology of the second phase. An improved match between experimental and calculated results could be obtained with the knowledge of the mechanism controlling the work hardening saturation.

ACKNOWLEDGMENTS

The author wishes to thank professors E. R. Parker and V. F. Zackay for their encourgement during the progress of this work. This work has been done under the auspices of the United States Atomic Energy Commission through the Inorganic Materials Research Division of the Lawrence Berkeley Laboratory.

REFERENCES

1. T. B. Massalski and H. W. King: J. Inst. of Metals, 1960-61 Vol. 89, p. 169.
2. A. K. Sinha and W. Hume-Rothery: JISI, 1967, Vol. 205, p. 671.
3. M. Hansen: Constitution of Binary Alloys, 2nd Ed., p. 720, McGraw-Hill Book Co., New York, 1965.
4. H. J. Goldschmidt: Research, 1957, Vol. 10, p. 289.
5. K. Kuo: Acta Met., 1953, Vol. 1, p. 720.
6. R. P. Elliott: (1954), T. R. No. 1, Contract AF 18(600)-642 Project No. B053.
7. H. J. Walbaum: Z. Krist, 1941, A103, p. 391.
8. R. P. Elliott: Constitution of Binary Alloys, 1st Suppl., p. 255, McGraw-Hill Book Co., New York 1958.
9. A. E. Dwight: Trans. ASM, 1961, Vol. 53, p. 479.
10. P. Paufler and G. E. R. Schulze: Monatsberichte, 1970, p. 67.
11. G. Sasaki: Mechanical Properties of Laves Phases, Dec. 1970, Univ. of Calif., Lawrence Berkeley Laboratory, UCRL-20301.
12. M. F. Ashby and R. Ebeling: Trans. AIME, 1966, Vol. 236, p. 1396.
13. J. Waldman, M. Schwartz and S. Nash: Trans. ASM, 1969, Vol. 62, p. 819.
14. R. W. Cahn: Recrystallization, Grain Growth and Textures, p. 113, American Society for Metals, Ohio, 1965.
15. M. F. Ashby: Phil Mag. 1966, 14, p. 1157.
16. J. L. Fisher, F. W. Hart and R. H. Pry, 1953, Acta Met., 1, p. 336.
17. E. Orowan: Symposium on Internal Stresses in Metals and Alloys, 1948, The Inst. of Metals, London, p. 451.

18. F. R. N. Nabarro: Proc. Phys. Soc. 1946, 58, p. 669.
19. M. F. Ashby: Physics of Strength and Plasticity, A. S. Argon, Ed., p. 113, The M. I. T. Press, Massachusetts, 1970.
20. V. F. Kocks, Phil. Mag. 1966, 13, p. 541.
21. R. Ebeling and M. F. Ashby: Phil. Mag., 1966, 13, p. 805.
22. R. L. Jones and A. Kelly: Proc. 2nd Bolton Landing Conf. on Oxide Dispersion Strengthening, G. S. Ansell, T. D. Cooper and F. V. Lenel, Ed., p. 229, Gordon and Breach, New York. 1968.
23. D. Dew-Hughes and W. D. Robertson; Acta Met., 1960, 8, p. 147.
24. A. Kelly and R. B. Nicholson: Prog. in Matl. Sci., B. Chalmers, Ed., p. 149, The MacMillan Co., New York, 1963.
25. G. Sachs: Z. Verein Deut. Ing., 1828, Vol. 72, p. 734.
26. G. I. Taylor: J. Inst. of Metals, 1938, Vol. 62, p. 307.
27. G. I. Taylor: Deformation and Flow of Solids, p. 3, Springer, 1956.
28. J. W. Hutchinson, J. Mech. Phys. Sol., 1964, Vol. 12, p. 25.
29. G. Y. Chin and W. L. Mammel: Trans. TMS-AIME, 1967, Vol. 239, p. 1400.
30. A. S. Keh: Phil. Mag., 1965, Vol. 12, p. 9.
31. L. J. Cuddy and W. C. Leslie: Second International Conf. on the Strength of Metals and Alloys, p. 258, American Society for Metals, 1970.
32. R. H. Jones: To be published.
33. E. W. Hart: Relation of Properties to Microstructure, ASM, 1953, p. 95.
34. A. M. Safdar and V. A. Philips: Trans. AIME, 1959, 215, p. 340.
35. P. B. Hirsch and T. E. Michell: Can. J. Phys., 1967, Vol. 45, p. 663.

36. A. S. Keh and S. Weissman: Electron Microscopy and Strength of Crystals, p. 231, G. Thomas and J. Washburn, Eds., J. Wiley and Sons, New York, 1963.

37. H. Conrad, S. Feuerstein and L. Rice: Aerospace Report No. TR-1001 (2250-20)-6, Aerospace Corp., El Segundo, Calif., April, 1967.

38. A. Kochendorfer and M. Swanson: Arch. Eisenhuttenw, 1960, vol. 31, p. 549.

Table I. Data on Average Particle Diameters, Interparticle Spacing, Volume Fractions and Compositions of Alloys

Alloy	$\bar{D}$(Å)	σ(Å)	λ(Å)	λ-$\bar{D}$(Å)	f(%)	at. % Ta
1						0
2	1250	450	5640	4390	0.73	0.41
3	1575	475	4970	3395	1.44	0.70
4	1825	800	4110	2285	3.08	1.00
5	2300	875	4380	2025	4.14	1.52
6	2050	990	3440	1390	5.32	2.05
7	1600	680	2470	870	6.14	2.53

Table II. Typical Purity of Iron and Tantalum Starting Materials

	Iron	Tantalum
Al	.001	
Be	.0005	
Ca	.001	.003
C	.002	.004
Cr	.001	
Co	.001	
Cu	.004	
Fe		.003
H	.01	.001
Pb	.001	
Mg	.0005	.006
Mn	.0015	
Mo	.004	.02
Nb		.10
Ni	.001	
N	.004	.004
O	.04	.005
P	.002	
Si	.003	.003
S	.003	
Ta	.001	
Sn	.003	
W	.001	.05

Table II. continued,

	Iron	Tantalum
V	.001	
Zn	.001	
Zr		.005

Table III. Lattice Parameter Data for the Compound Fe_2Ta

$a_o(A^o)$	$c_o(A^o)$	c/a	Reference
4.806	7.846	1.633	This work
4.828	7.838	1.624	3
4.816	7.868	1.633	5
4.817	7.822	1.624	6
4.81	7.85	1.63	7
4.80	7.84	1.63	ASTM Powder Diffraction File for Fe_7Ta_3.

Table IV. Interplanar Spacings and Intensities for the Fe-Ta Laves Phase.

Fe-2 at.% Ta alloy 5 hr-800°C			ASTM Powder Diff. File for Fe_7Ta_3	
hk·ℓ	$d(A^o)$	I/I(11·2)	$d(A^o)$	I/I(11·2)
10·0	4.122	10	4.15	15
00·2	3.893	5	3.91	5
10·1	3.655	10	3.68	10
10·2	2.838	10	2.85	20
11·0	2.391	75	2.398	80
10·3	2.204	80	2.212	100
20·0	2.074	30	2.078	30
11·2	2.042	100	2.047	100
20·1	2.006	65	2.010	70
00·4	1.957	15	1.957	5
20·3	1.625	15		
21·0	1.570	25		
30·0	1.386	25	1.386	20
21·3	1.347	50	1.346	50
20·3,00·6	1.307	45	1.307	30
20·5	1.252	35		
22·0	1.201	35		

Table V. Comparison of Calculated and Experimental Yield Strength Data

Alloy	σ_y (kg/mm^2) proportional limit	σ_y 0.2% (kg/mm^2)	σ_y (kg/mm^2) calculated	$\frac{0.85\ MGb\phi}{2\pi(\lambda-D)}$ Exp	Calc
1	5.5	18.8	16.3		
2	15.5	20.0	20.0	$11.1\times10^{-5}\ \frac{kg-cm}{mm^2}$	$9.75\times10^{-5}\ \frac{kg-cm}{mm^2}$
3	16.6	20.0	20.0		
4	22.7	28.1	27.7		
5	26.3	31.4	31.7		
6	26.6	32.9	42.9		
7	22.1	28.5	61.6		

Table VI. Comparison of Calculated and Experimental Work Hardening Data and Ultimate Stress.

Alloy	$M^{3/2}CG(\frac{bf}{D})$ Exp.	Calc.	% Diff.	$\Delta\sigma_h$ max(kg/mm^2)	σ_u (kg/mm^2) Exp.	Calc.	% Diff.
2	75.5	67.8	10	6.5	37.2	42.9	14
3	95.5	84.7	10	10.5	40.5	47.2	15.5
4	115.0	115.0	0	13.0	46.5	60.2	26
5	112.0	119.0	6	12.3	50.0	65.8	27
6	138.0	143.0	4	16.5	55.0	74.1	30
7	159.0	174.0	10	20.5	56.0	79.9	35

FIGURE CAPTIONS

Fig. 1. Schematic of heat treatment given to Fe-Ta alloys.

Fig. 2. Iron rich portion of the Fe-Ta phase diagram. (After Sinha and Hume-Rothery[2]).

Fig. 3. Lattice parameter of iron versus atomic percent tantalum, in single phase and two phase condition.

Fig. 4. Scanning electron micrographs showing spheroidization of grain boundary phase in alloy 6. a) aged condition b) after 12 min. at 1100°C.

Fig. 5. Micrographs of carbon extraction replicas showing Laves phase particles of two phase iron alloys. a) Alloy 2 b) Alloy 3 c) Alloy 4 d) Alloy 5 e) Alloy 6 f) Alloy 7

Fig. 6. Optical micrographs showing prior α grain boundary and matrix Laves phase in two phase iron alloys. a) Alloy 2 b) Alloy 3 c) Alloy 4 d) Alloy 5 e) Alloy 6 f) Alloy 7

Fig. 7. Cumulative probability versus particle diameter of Laves phase particles extracted from two phase iron alloys. a) Alloy 2 b) Alloy 3 c) Alloy 4 d) Alloy 5 e) Alloy 6 f) Alloy 7

Fig. 8. The probability, P(r), versus r, where P(r) is the probability a square marked on an extraction replica contains r particles. a) Alloy 2 b) Alloy 3 c) Alloy 4 d) Alloy 5 e) Alloy 6 f) Alloy 7

Fig. 9. Micrograph of a typical X-ray Laue back reflection pattern of two phase iron alloys. Inner ring (110), outer ring (200)

Fig. 10. Optical micrographs showing the final α grain structure of two phase iron alloys. a) Alloy 2 b) Alloy 5

Fig. 11. Transmission electron micrographs showing orientation difference between two sub-grains in alloy 2 in undeformed condition.

Fig. 12. Transmission electron micrographs showing the dislocation structure of undeformed two phase iron alloys. a) Alloy 4 b) Alloy 6

Fig. 13. Transmission electron micrographs showing the dislocation structure of two phase iron alloys after a tensile strain a) Alloy 2, 20% strain b) Alloy 4, 12% strain

Fig. 14. The 0.2% yield stress versus the Orowan parameter $\frac{1}{(\lambda-\bar{D})} \ln\left(\frac{\bar{D}}{4b}\right)$.

Fig. 15. The work hardening, σ_h, versus the square root of the true plastic strain a) Alloys 1, 2, 3, 4 b) Alloys 5, 6 c) Alloy 7

Fig. 16. The work hardening, σ_h, versus the dimensionless parameter, $\left(\frac{bf\varepsilon}{\bar{D}}\right)^{1/2}$, for strains of 1%, 2.5% and 5%.

Fig. 17. The difference, $\Delta\sigma_h$, in the work hardening of single phase and two phase alloys versus the strain.

Fig. 18. Calculated and experimental true stress-true strain curves for two phase iron alloys up to 3% strain. a) Alloy 2 b) Alloy 3 c) Alloy 4 d) Alloy 5 e) Alloy 6 f) Alloy 7

Fig. 19. Calculated and experimental true stress-true strain curves for two phase iron alloys up to the ultimate stress a) Alloy 1 b) Alloy 2 c) Alloy 3 d) Alloy 4 e) Alloy 5 f) Alloy 6 g) Alloy 7

Fig. 20. True stress-true strain curves of polycrystalline copper and of single crystal copper near the ⟨111⟩ corrected to

to polycrystalline by the Sachs and Taylor models. (After Koehenclorfer and Swanson[38])

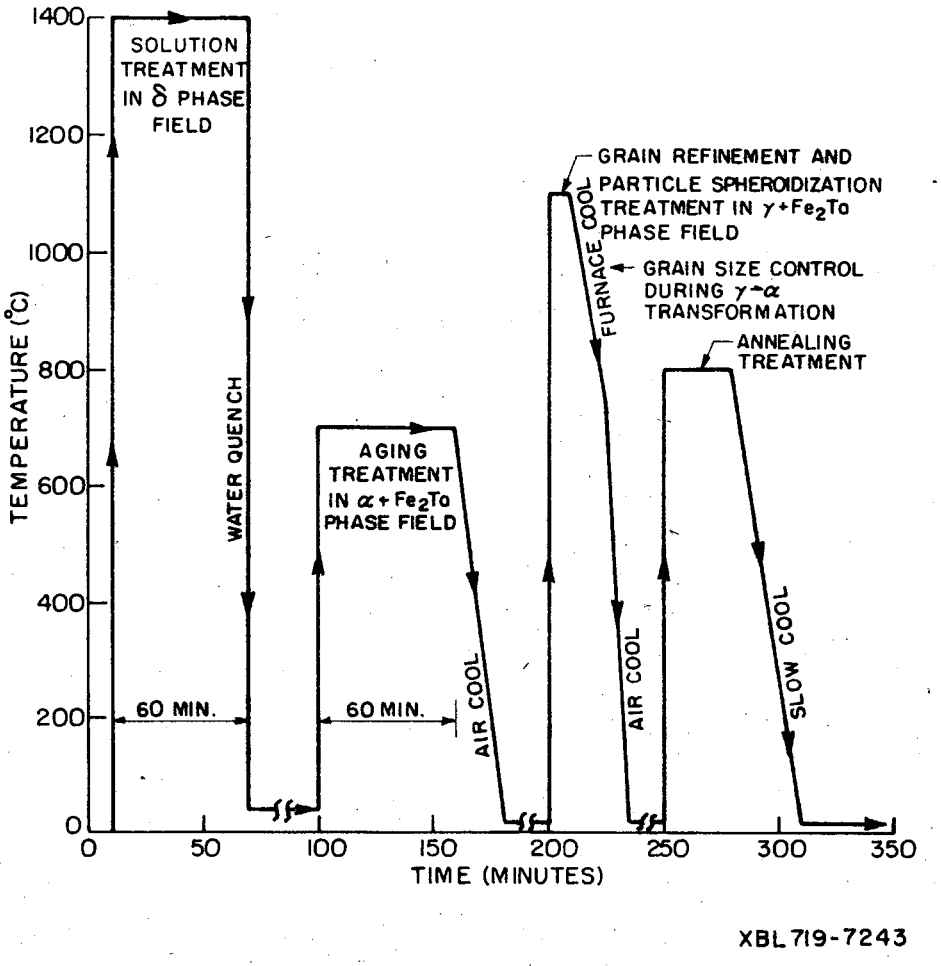

Fig. 1.

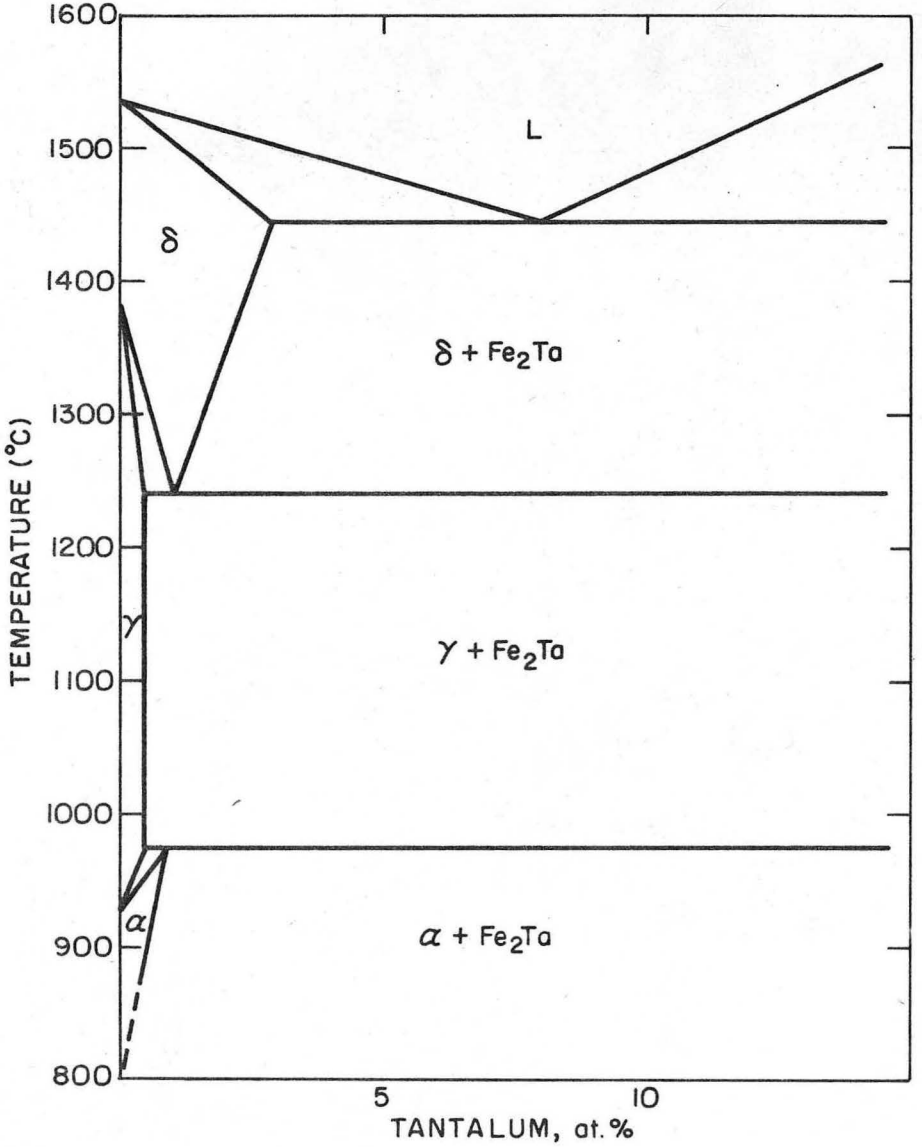

XBL 719-7223

Fig. 2.

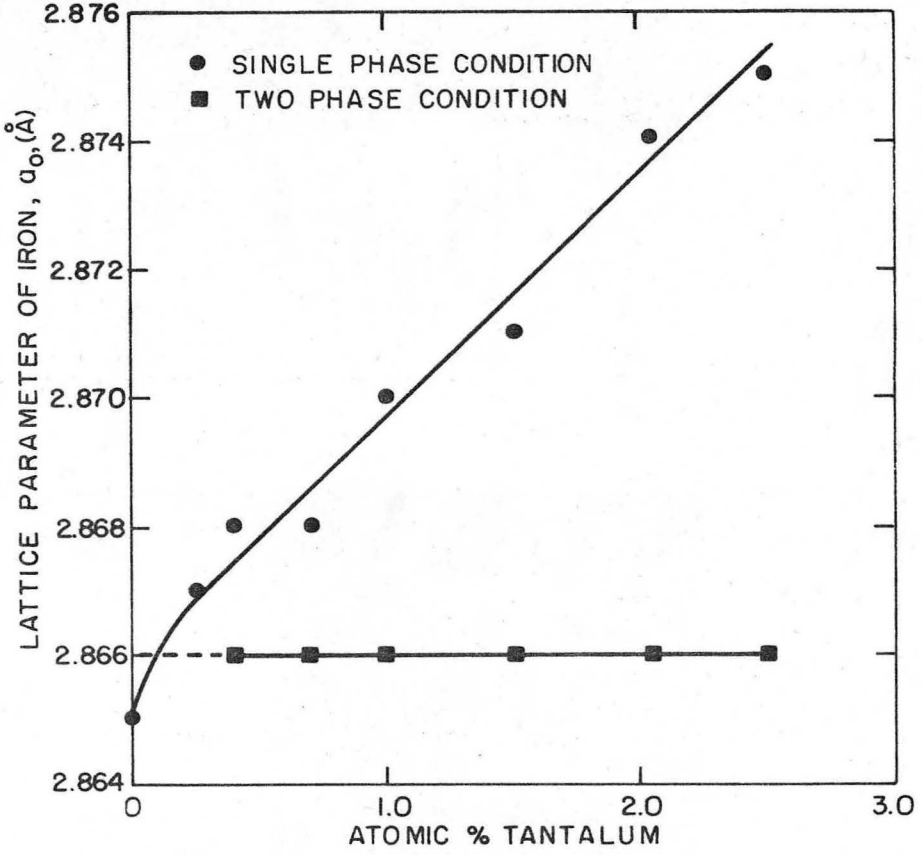

XBL719-7244

Fig. 3.

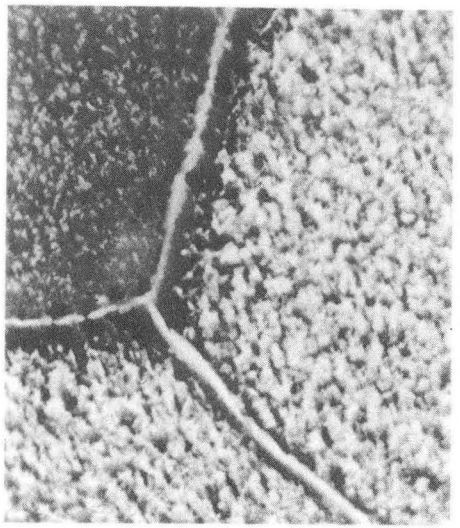

1μ

Fig. 4a.

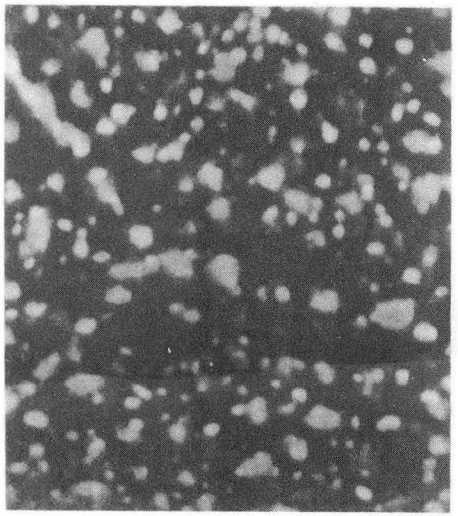

1μ

XBB 719-4459

Fig. 4b.

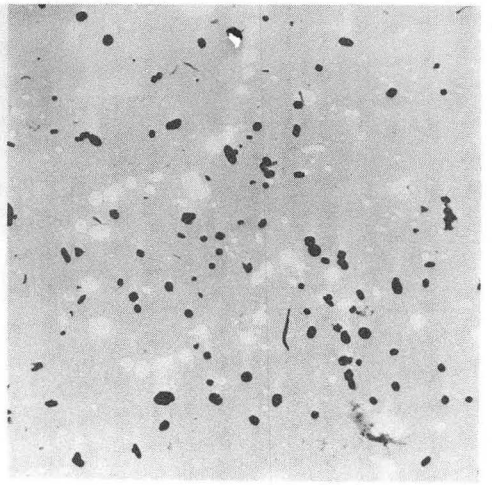

1μ

Fig. 5a.

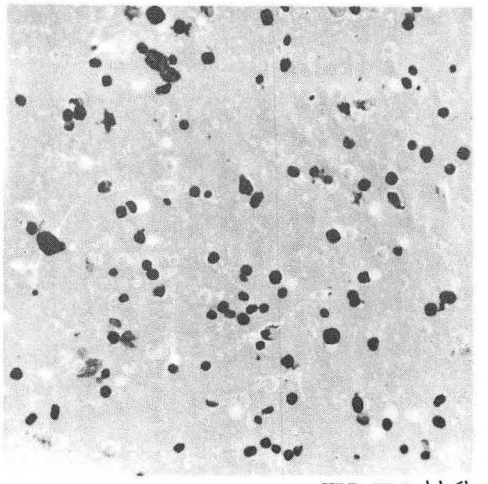

1μ

XBB 719-4464

Fig. 5b.

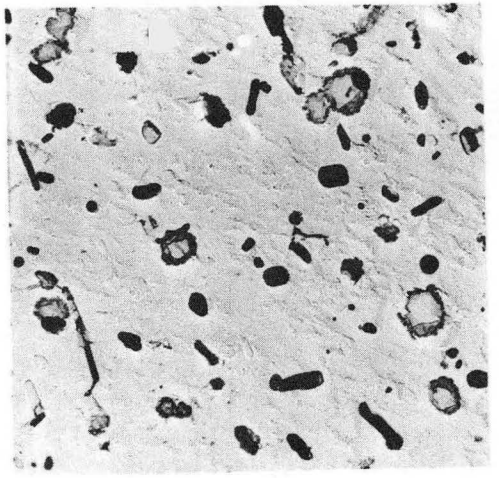

Fig. 5c.

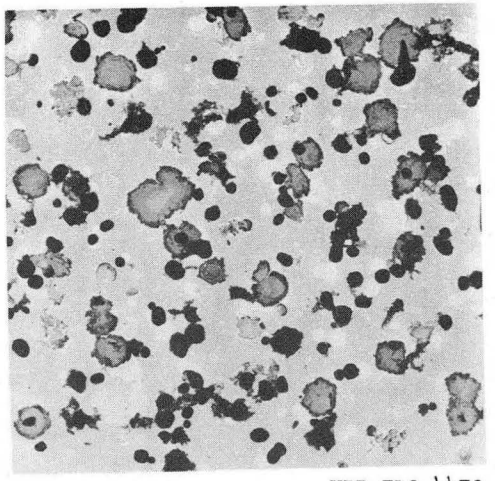

XBB 719-4470

Fig. 5d.

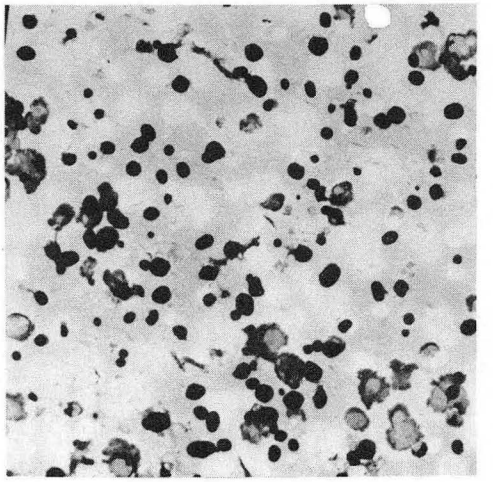

Fig. 5e.

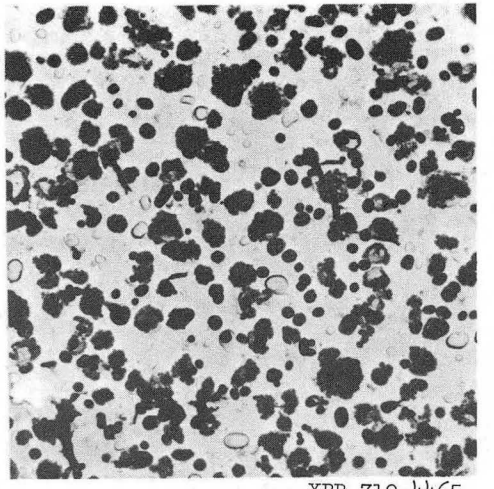

XBB 719-4465

Fig. 5f.

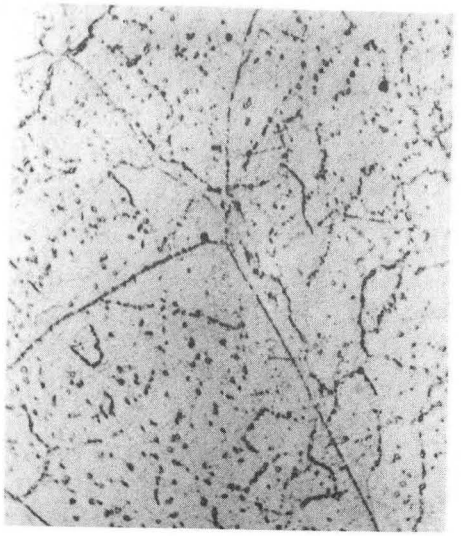

10μ

Fig. 6a.

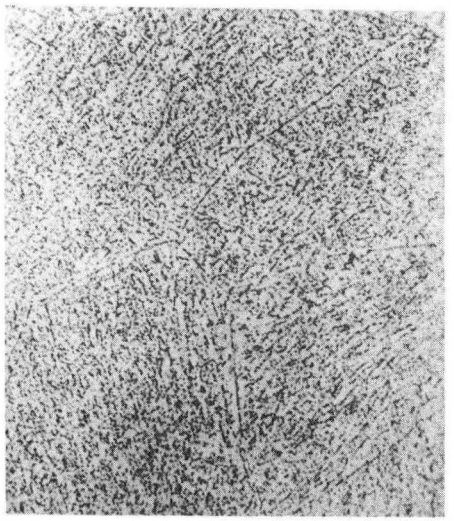

10μ

XBB 719-4463

Fig. 6b.

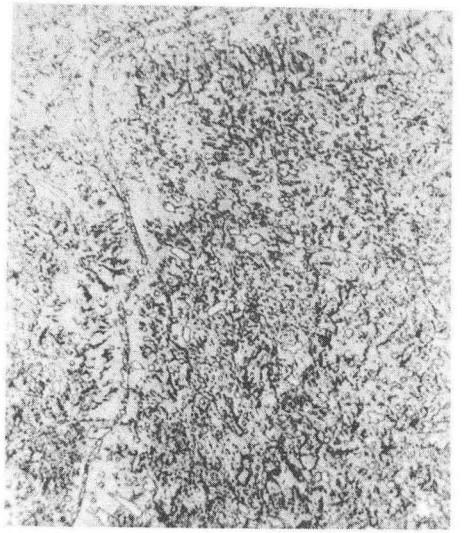

10μ

Fig. 6c.

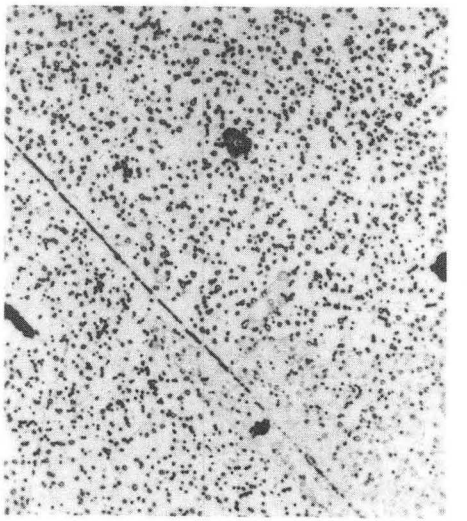

5μ

XBB 719-4462

Fig. 6d.

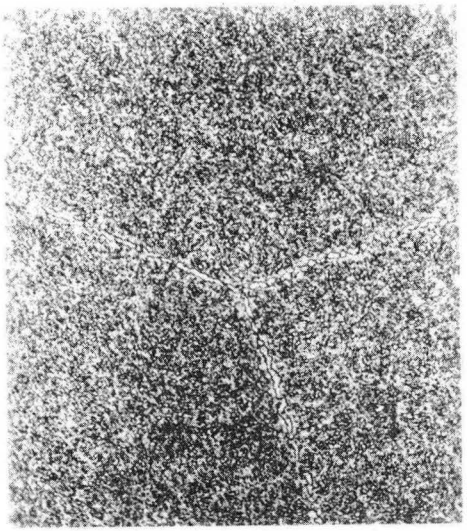

Fig. 6e.

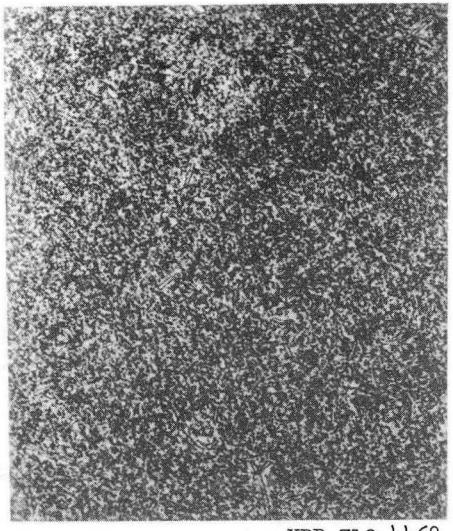

XBB 719-4468

Fig. 6f.

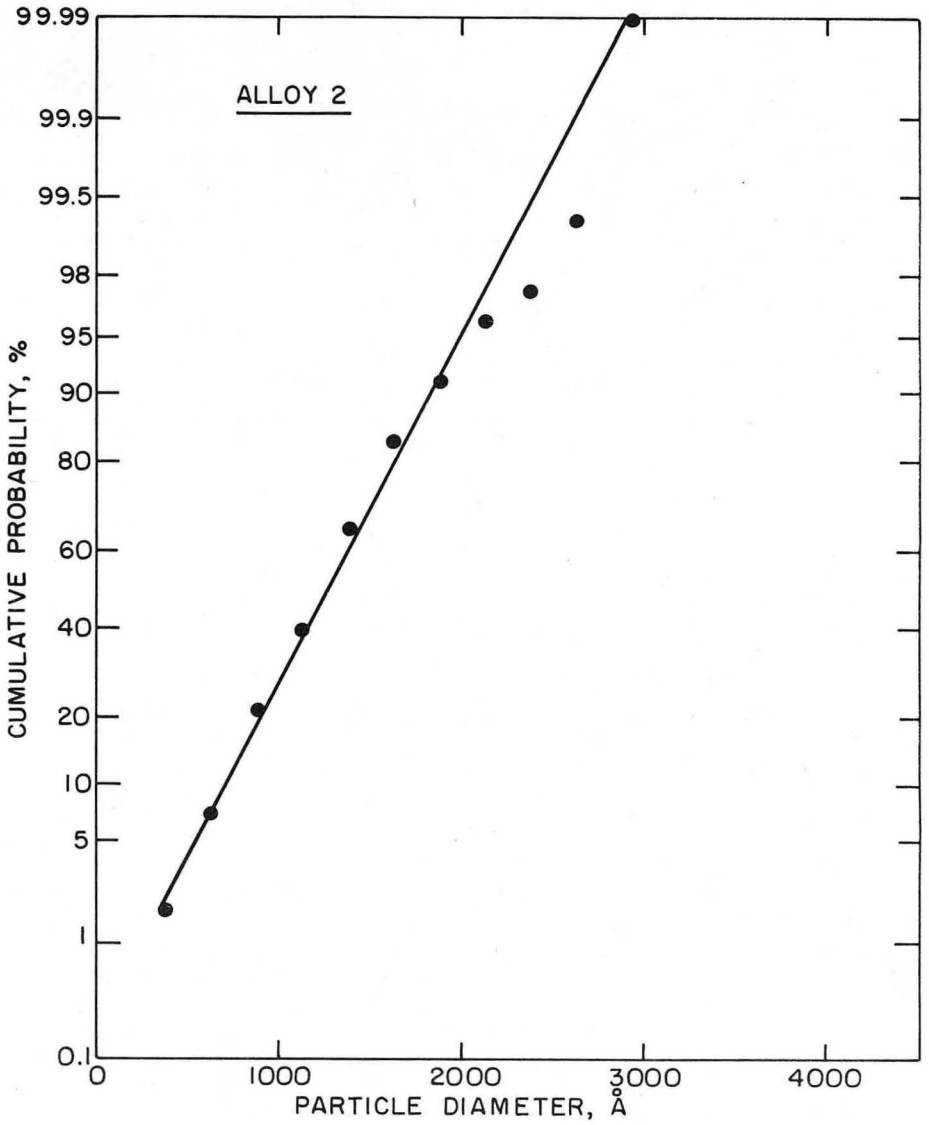

XBL 718-7142

Fig. 7a.

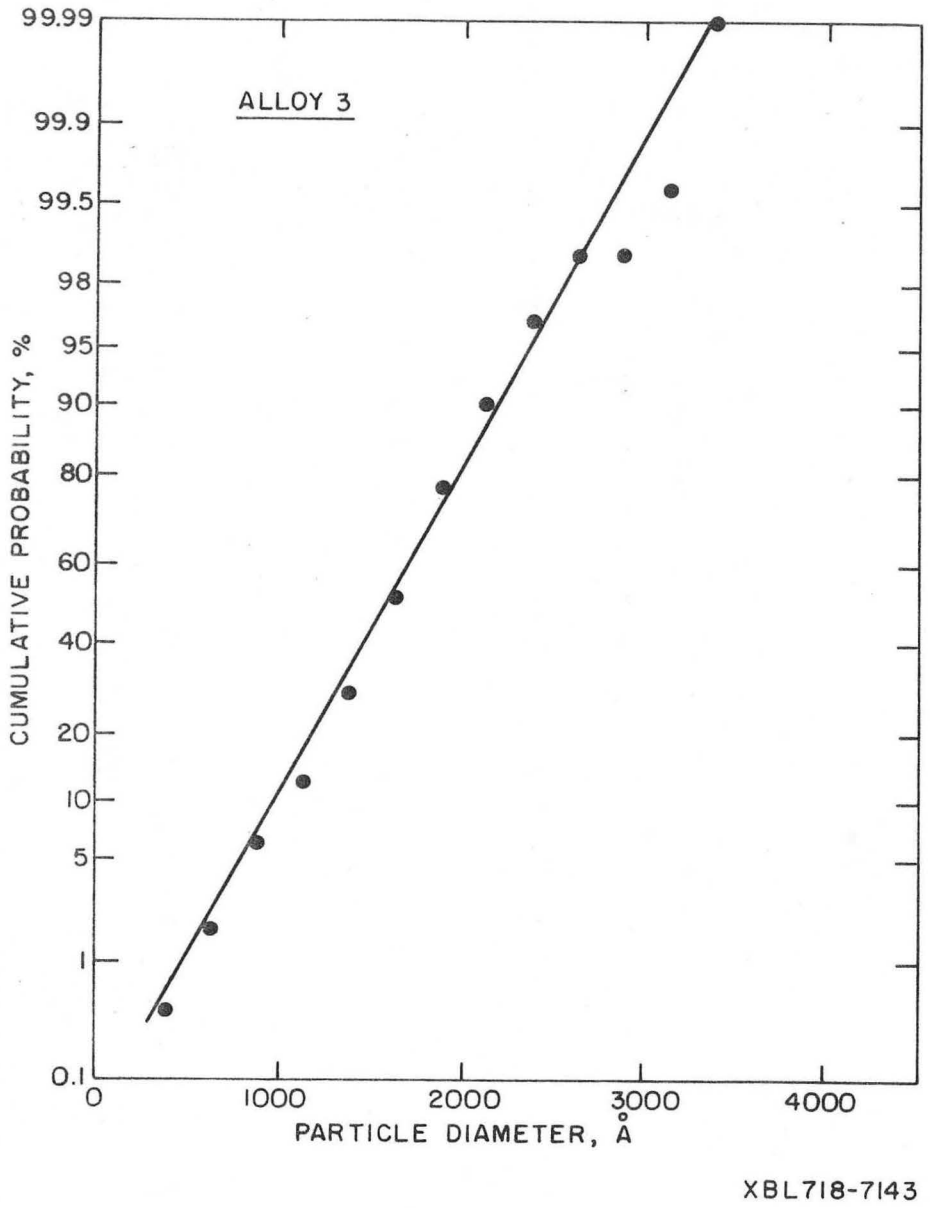
ALLOY 3
CUMULATIVE PROBABILITY, %
99.99
99.9
99.5
98
95
90
80
60
40
20
10
5
1
0.1
0
1000
2000
3000
4000
PARTICLE DIAMETER, Å
XBL718-7143

Fig. 7b.

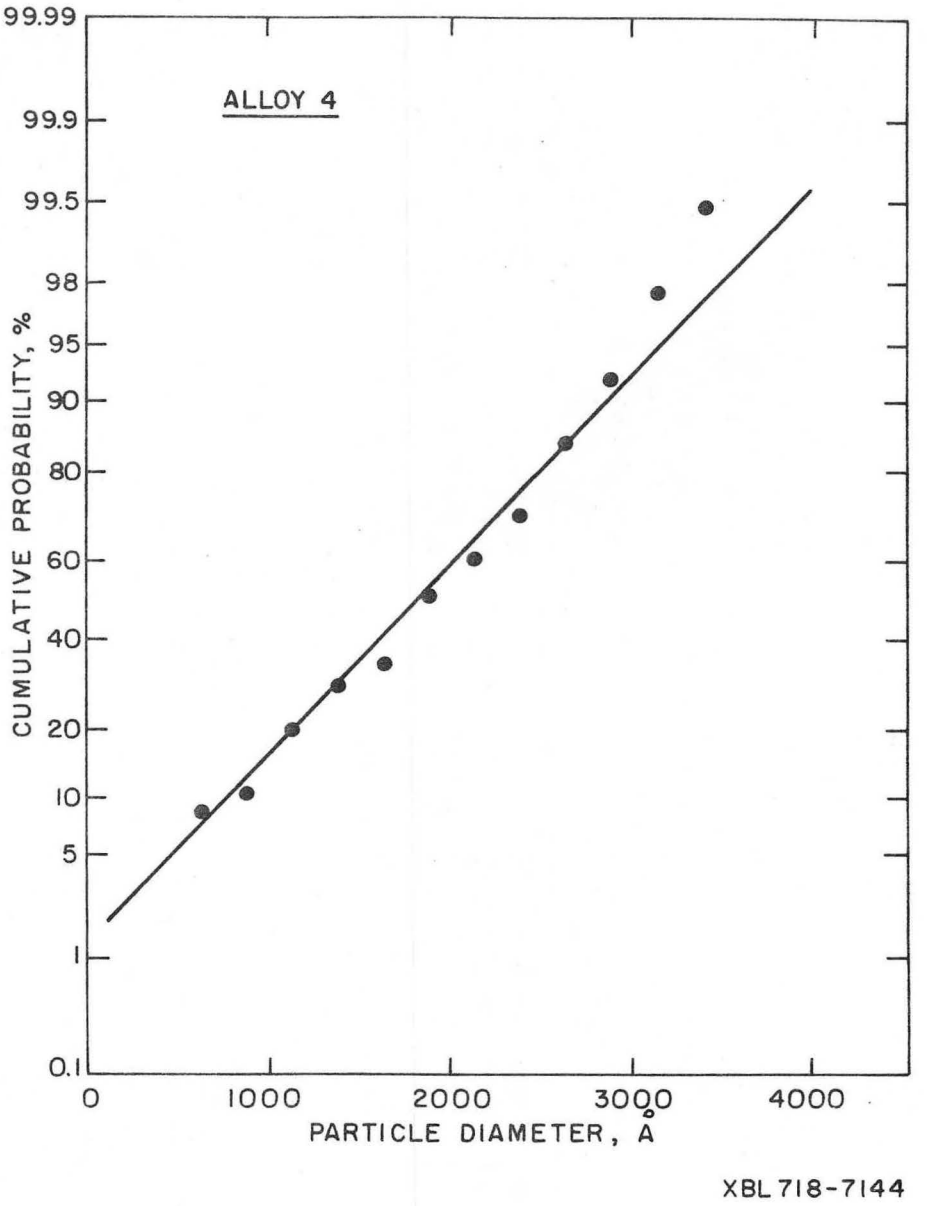
ALLOY 4
CUMULATIVE PROBABILITY, %
99.99
99.9
99.5
98
95
90
80
60
40
20
10
5
1
0.1
0
1000
2000
3000
4000
PARTICLE DIAMETER, Å
XBL718-7144

Fig. 7c.

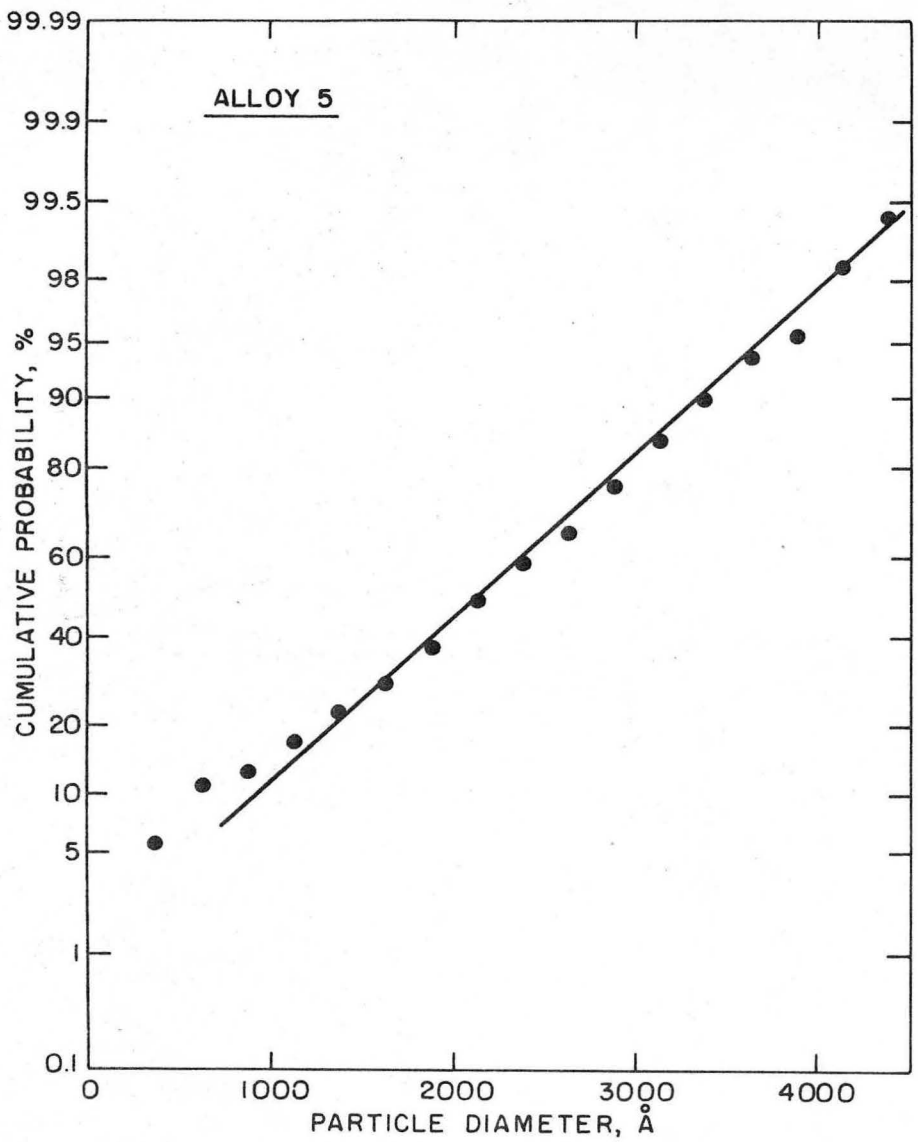
ALLOY 5
99.99
99.9
99.5
98
95
90
80
60
40
20
10
5
1
0.1
CUMULATIVE PROBABILITY, %
0
1000
2000
3000
4000
PARTICLE DIAMETER, Å
XBL 718-7145

Fig. 7d.

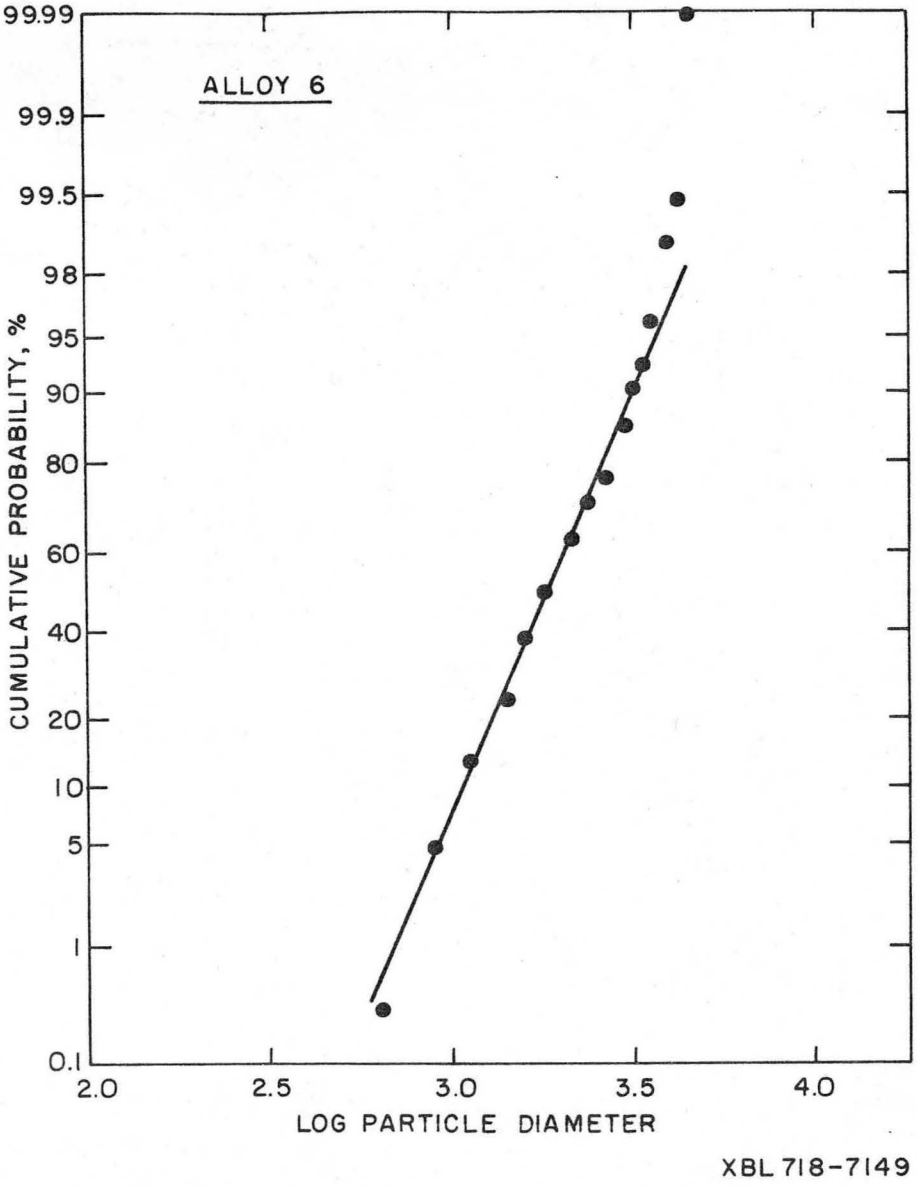
ALLOY 6
99.99
99.9
99.5
98
95
90
80
60
40
20
10
5
1
0.1
CUMULATIVE PROBABILITY, %
2.0
2.5
3.0
3.5
4.0
LOG PARTICLE DIAMETER
XBL 718-7149

Fig. 7e.

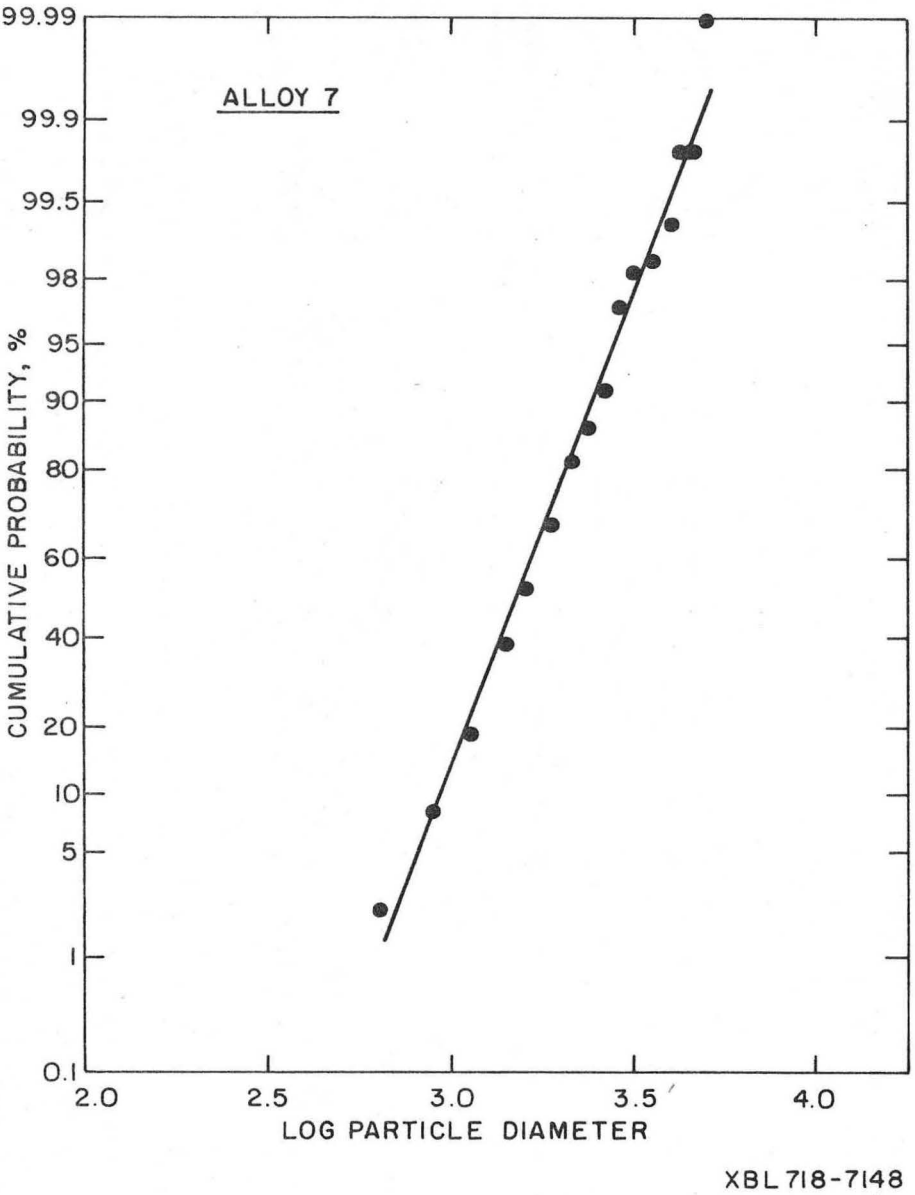
ALLOY 7
99.99
99.9
99.5
98
95
90
80
60
40
20
10
5
1
0.1
CUMULATIVE PROBABILITY, %
2.0
2.5
3.0
3.5
4.0
LOG PARTICLE DIAMETER
XBL 718-7148

Fig. 7f.

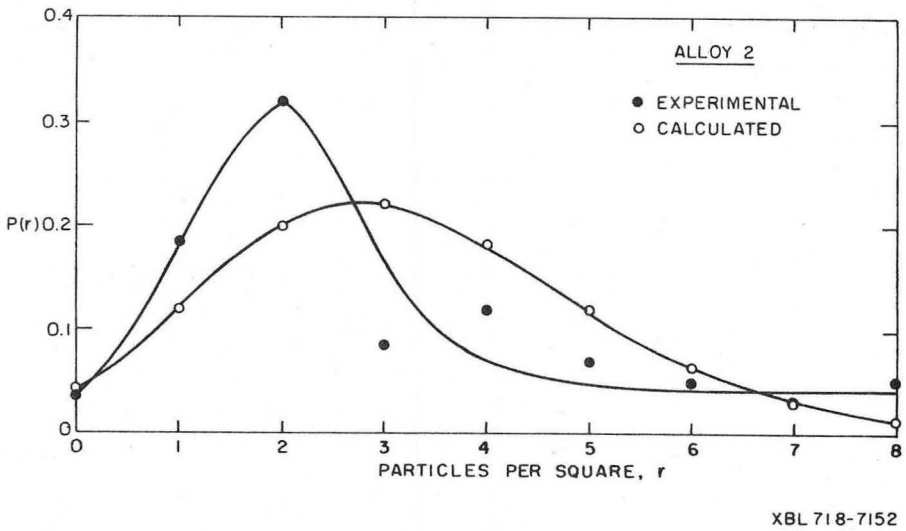
ALLOY 2
EXPERIMENTAL
CALCULATED
P(r)
0.4
0.3
0.2
0.1
0
0
1
2
3
4
5
6
7
8
PARTICLES PER SQUARE, r
XBL 718-7152

Fig. 8a.

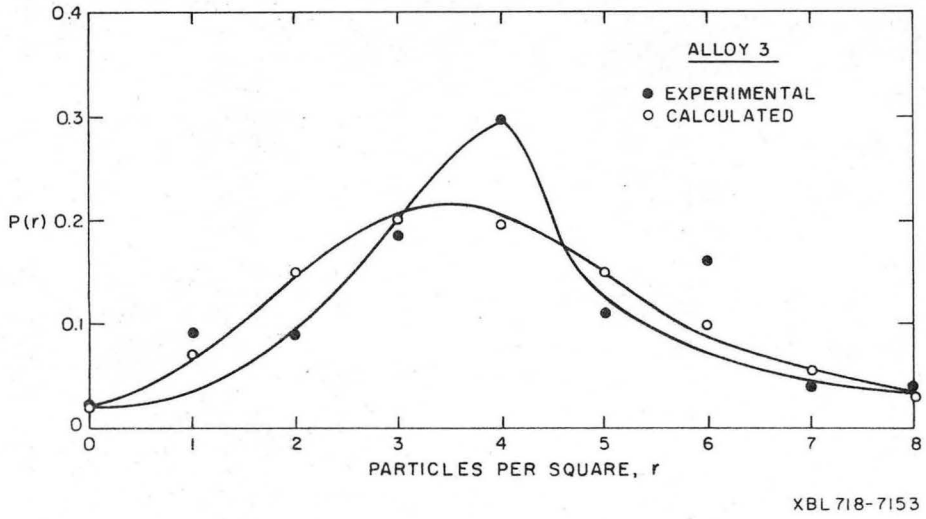
ALLOY 3
EXPERIMENTAL
CALCULATED
P(r)
PARTICLES PER SQUARE, r
XBL 718-7153

Fig. 8b.

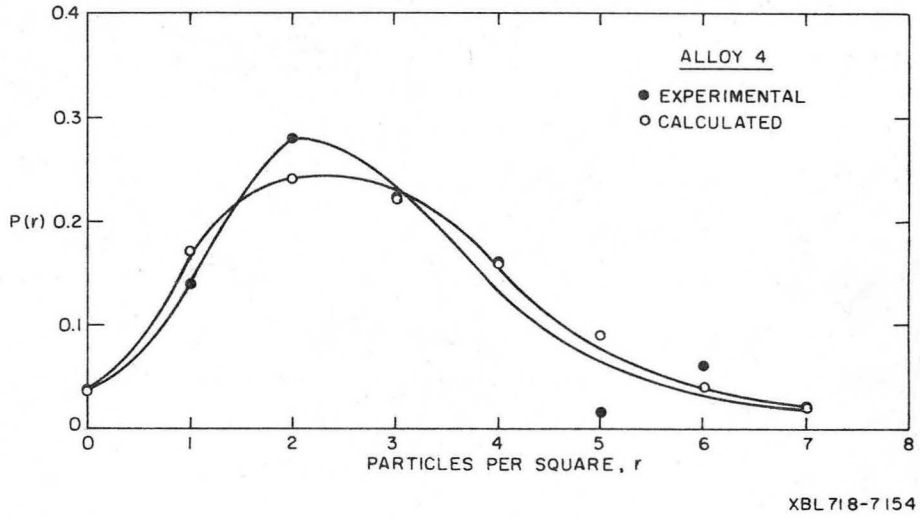
ALLOY 4
EXPERIMENTAL
CALCULATED
P(r)
PARTICLES PER SQUARE, r
XBL 718-7154

Fig. 8c.

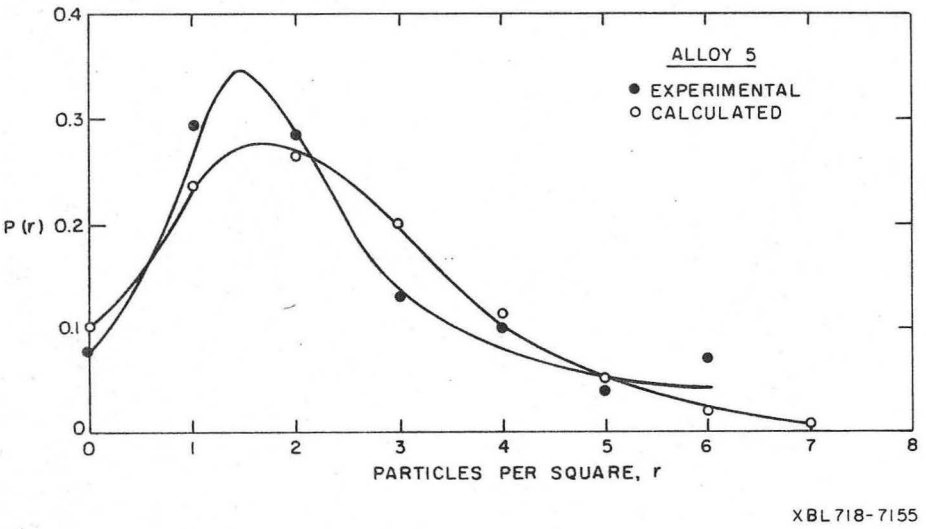
ALLOY 5
EXPERIMENTAL
CALCULATED
P (r)
PARTICLES PER SQUARE, r
XBL 718-7155

Fig. 8d.

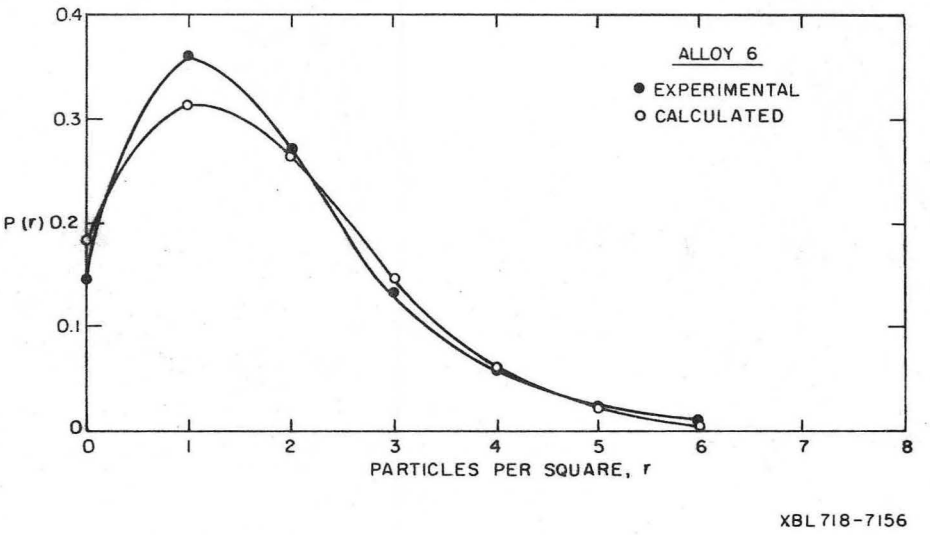
ALLOY 6
EXPERIMENTAL
CALCULATED
P (r)
PARTICLES PER SQUARE, r
XBL 718-7156

Fig. 8e.

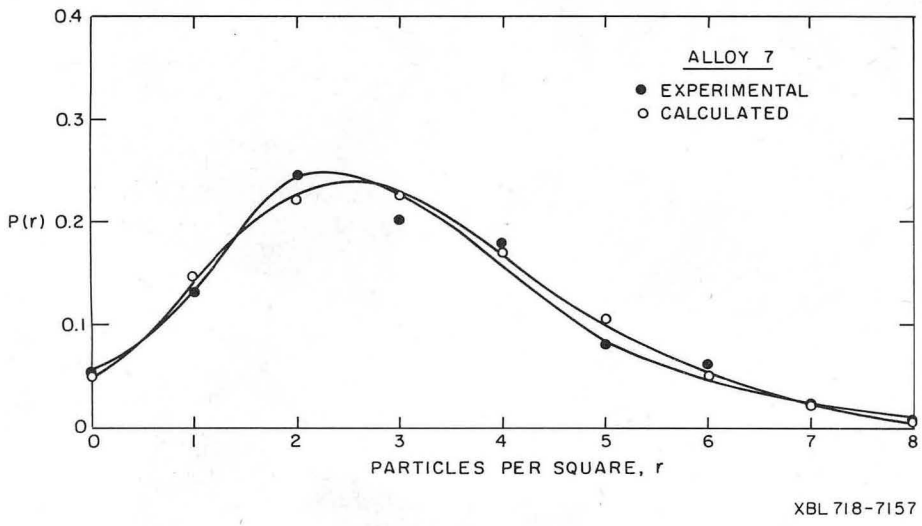

Fig. 8f.

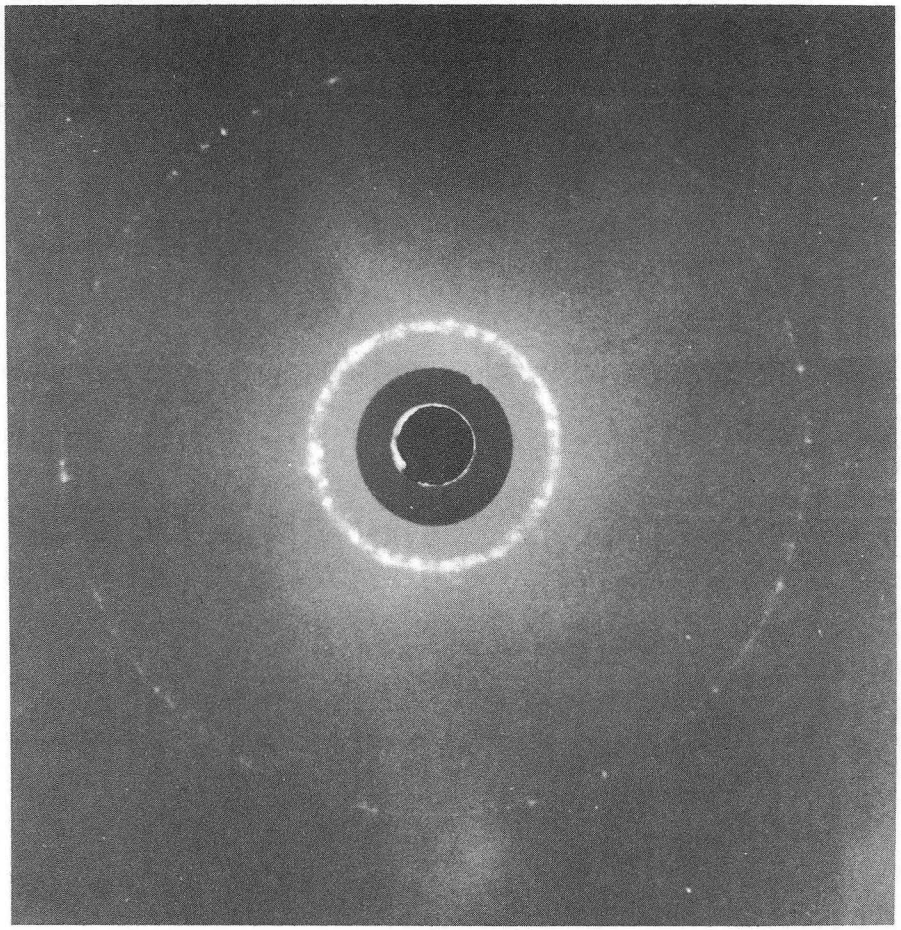

XBB 719-4458

Fig. 9.

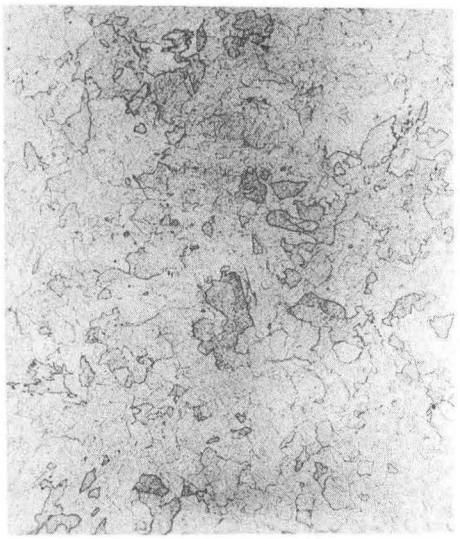

Fig. 10a.

XBB 719-4469

Fig. 10b.

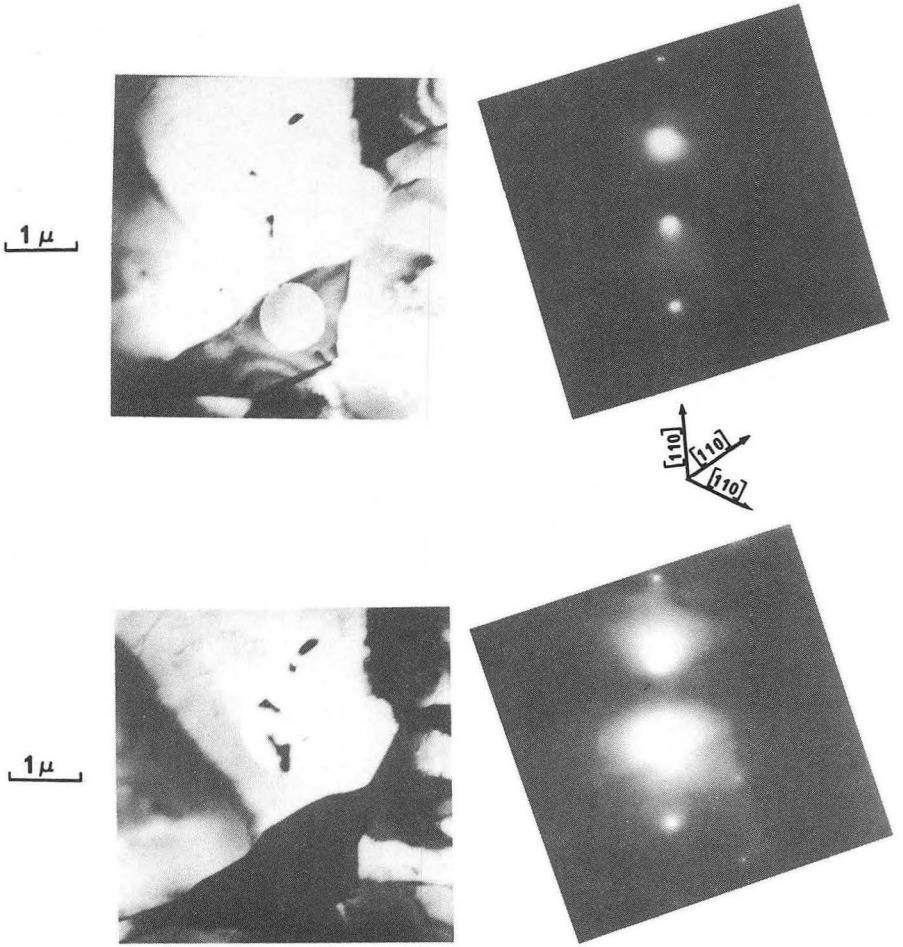

XBB 719-4461

Fig. 11.

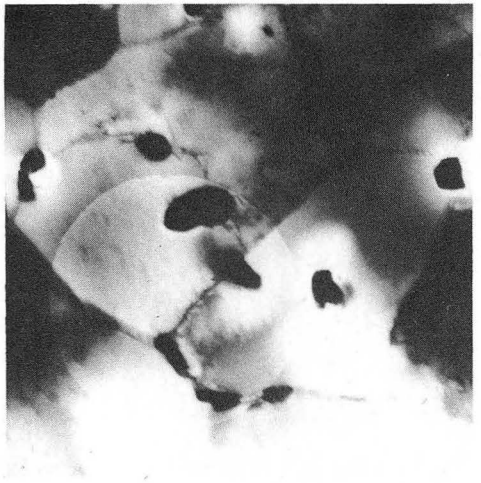

Fig. 12a.

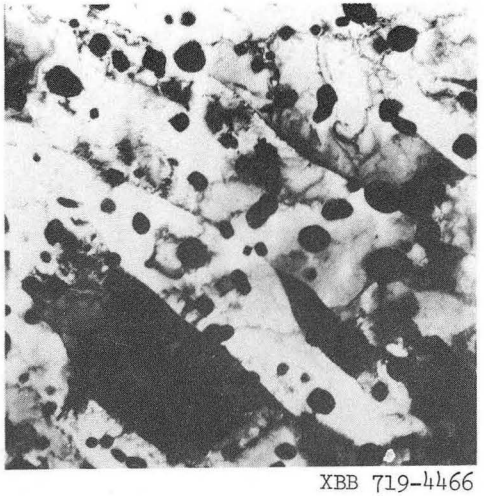

XBB 719-4466

Fig. 12b.

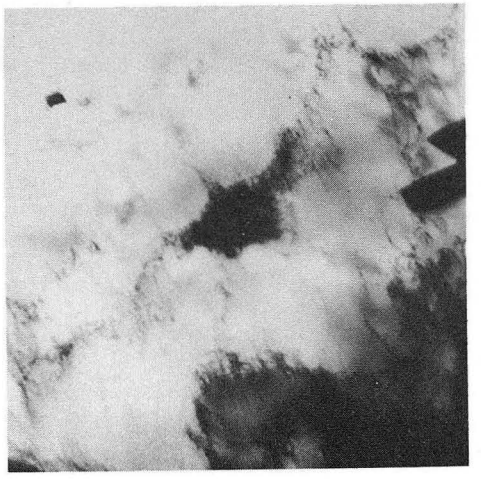

XBB 719-4460

Fig. 13a.

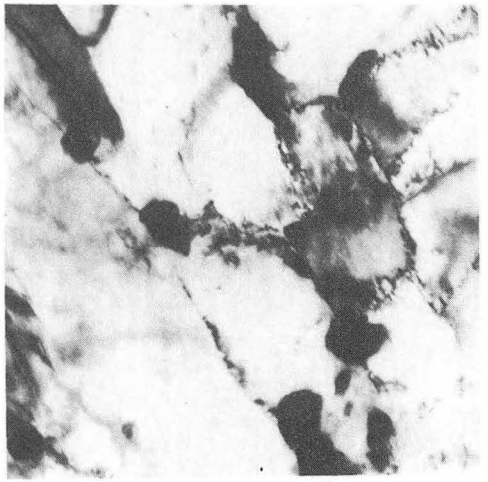

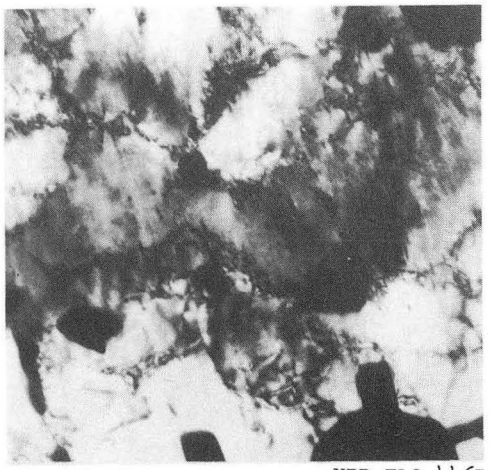

XBB 719-4467

Fig. 13b.

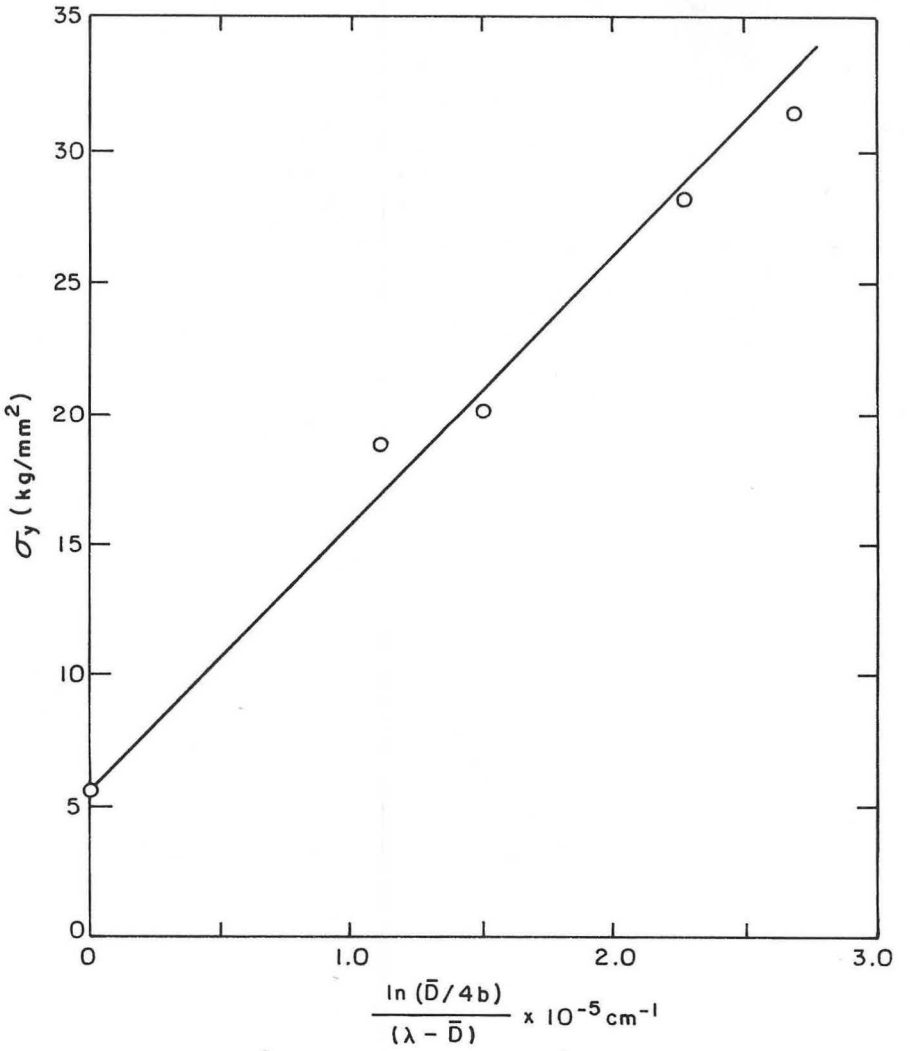

XBL 719-7301

Fig. 14.

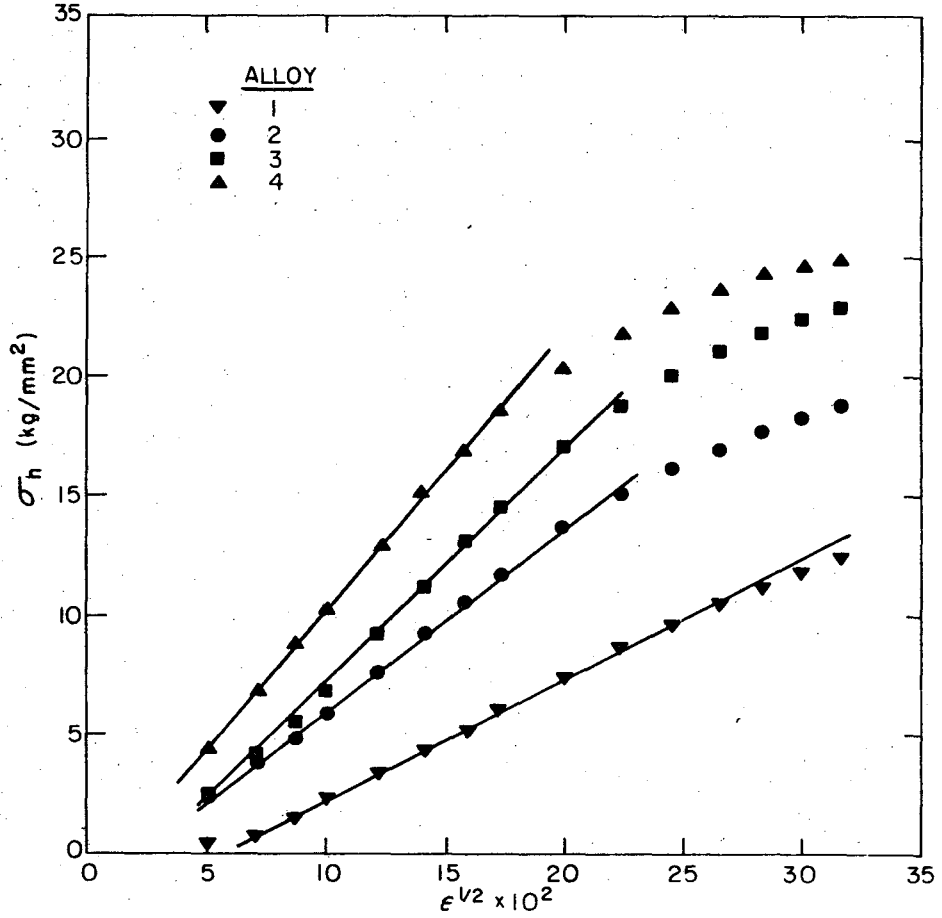

XBL719-7303

Fig. 15a.

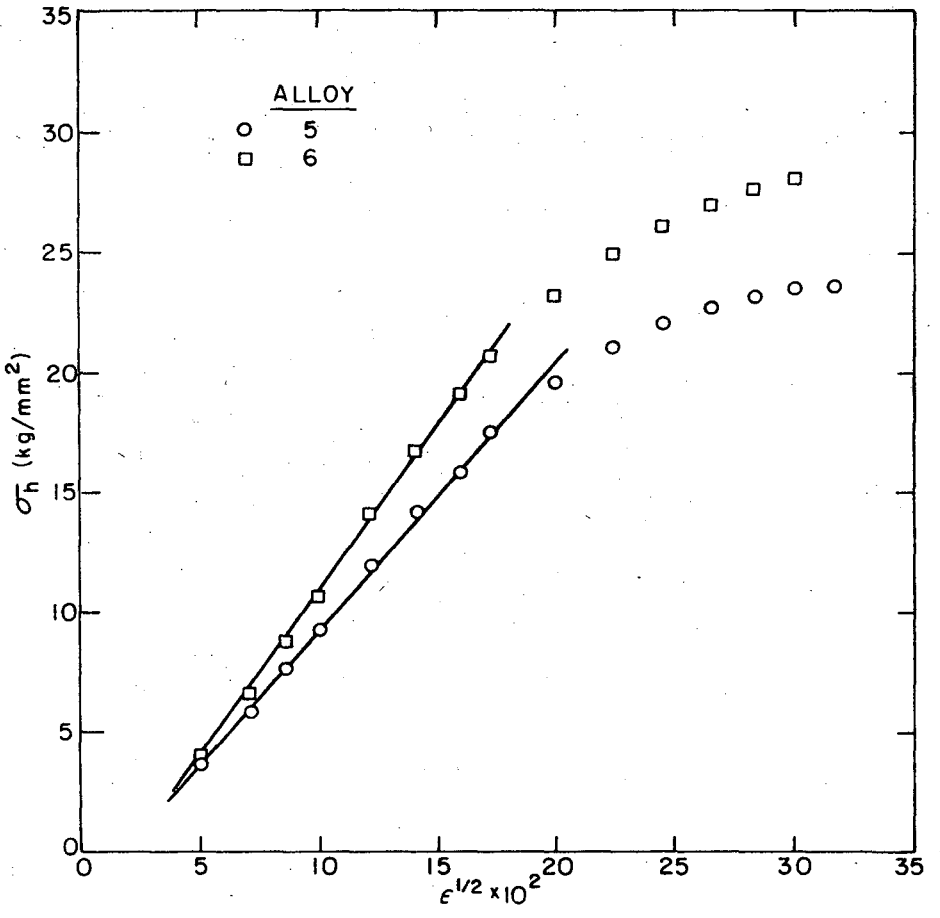

XBL719-7304

Fig. 15b.

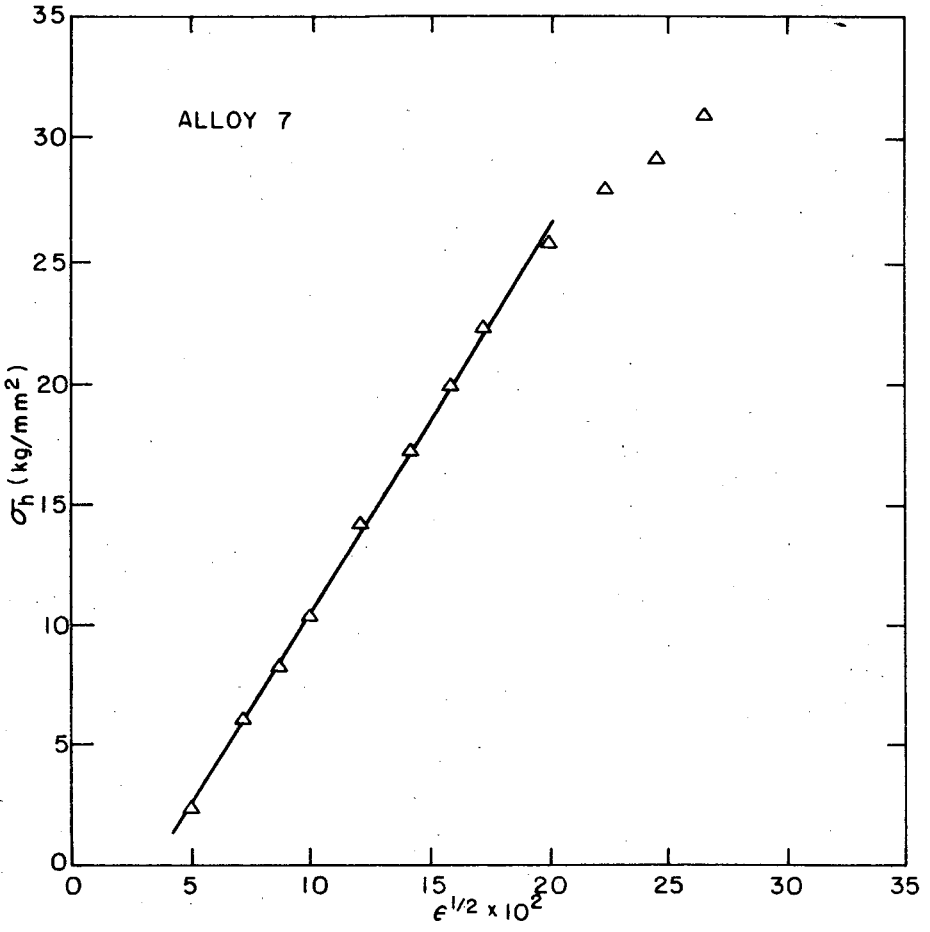

XBL 719-7305

Fig. 15c.

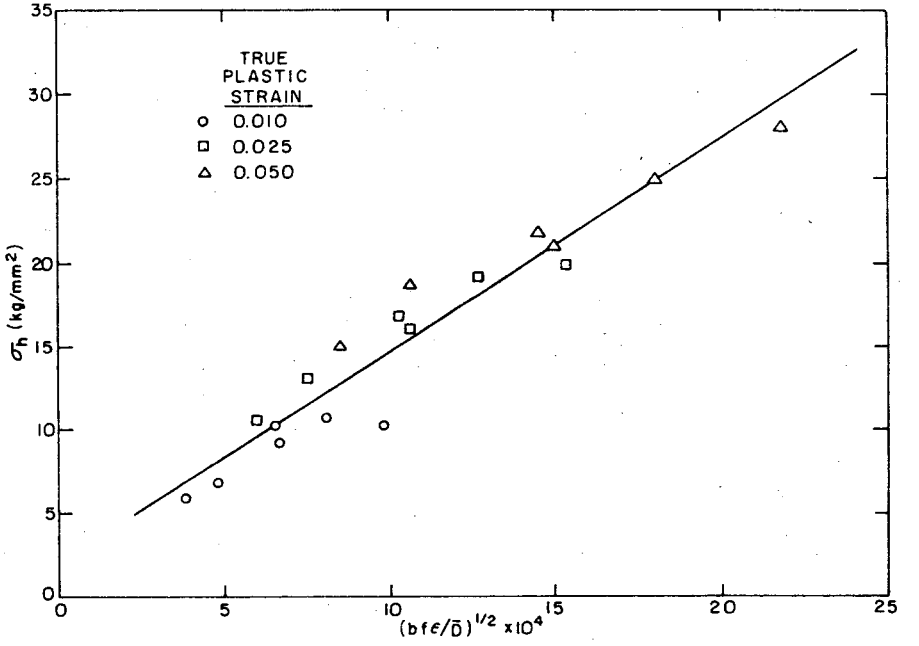

XBL 719-7302

Fig. 16.

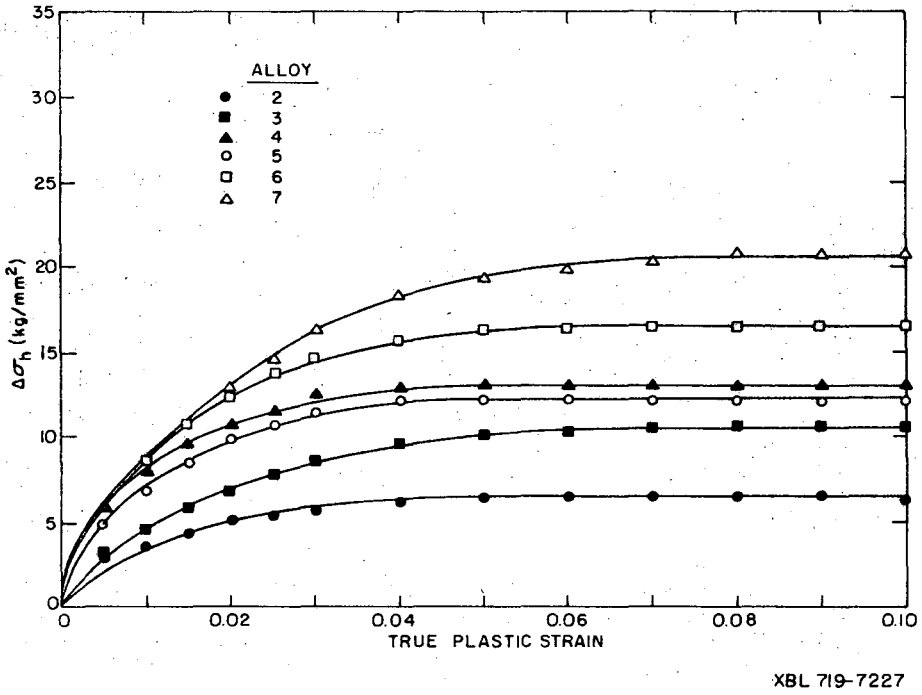

Fig. 17.

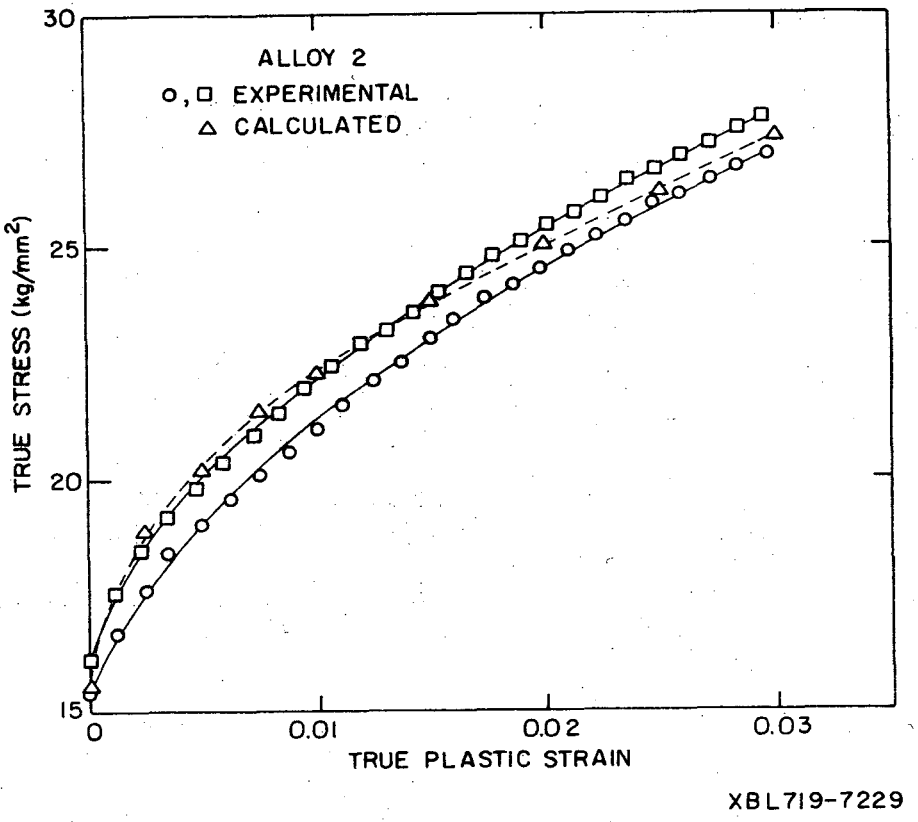

Fig. 18a.

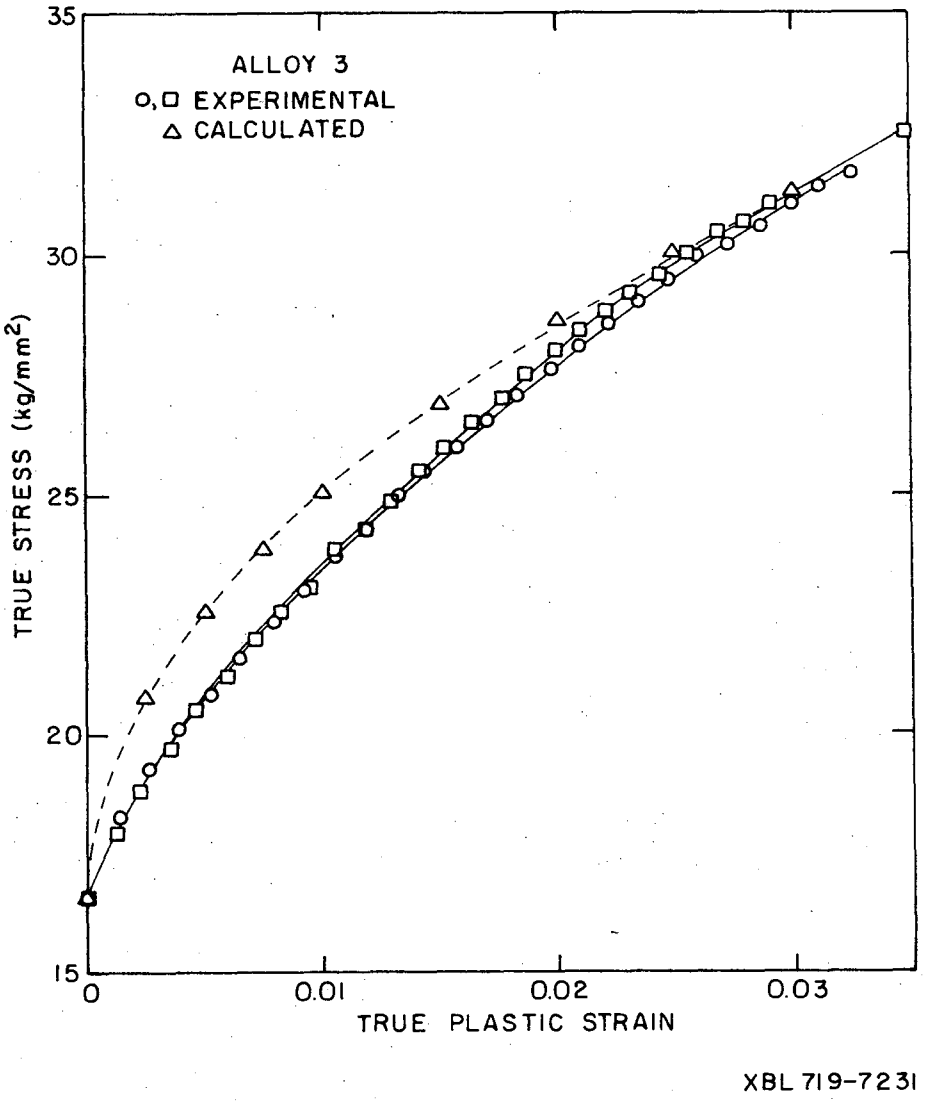

Fig. 18b.

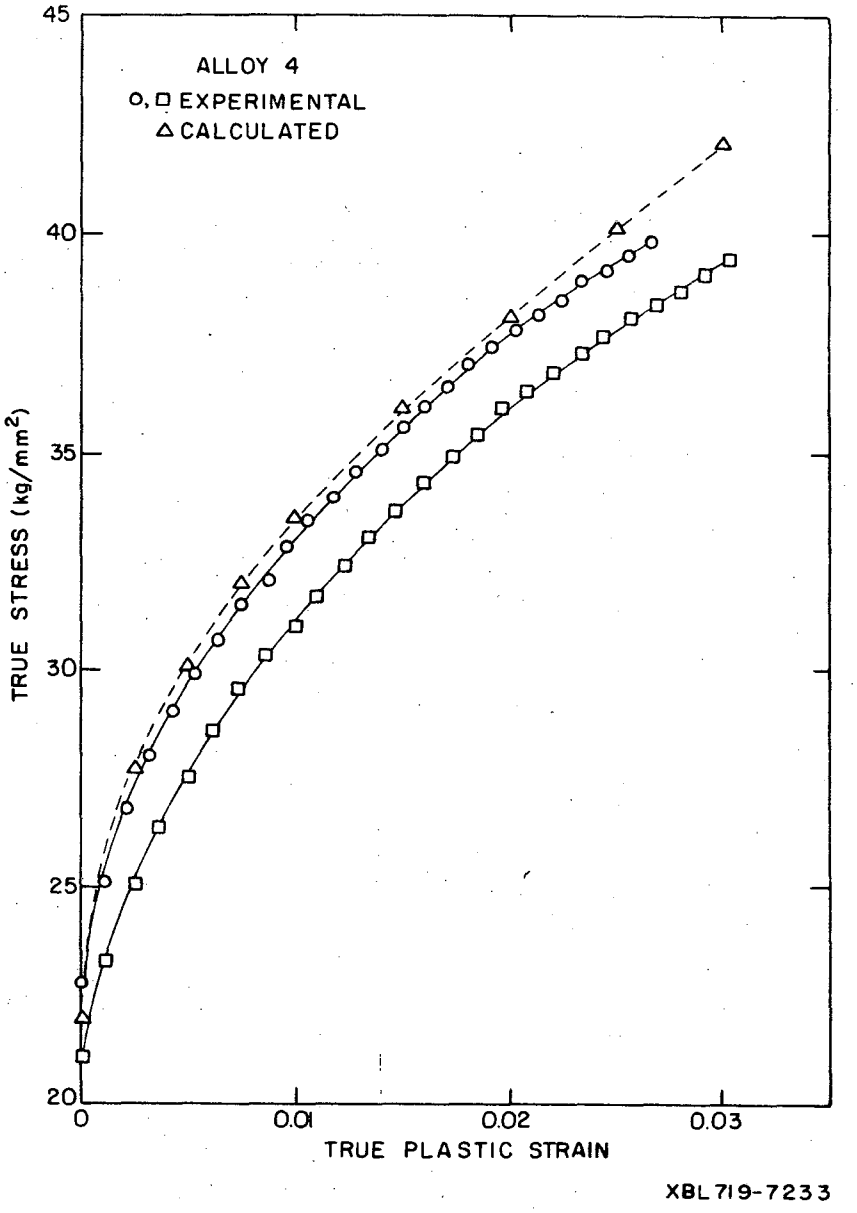

Fig. 18c.

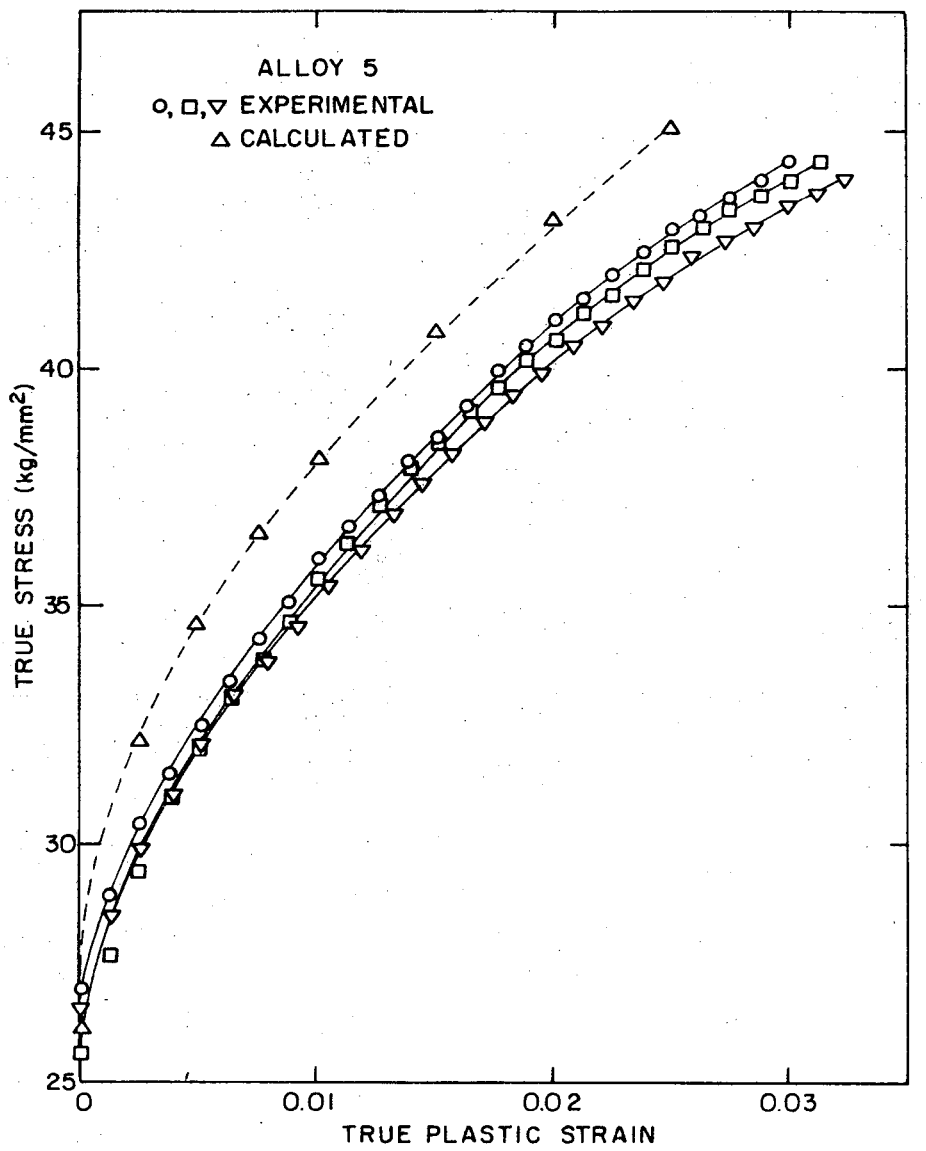

Fig. 18d.

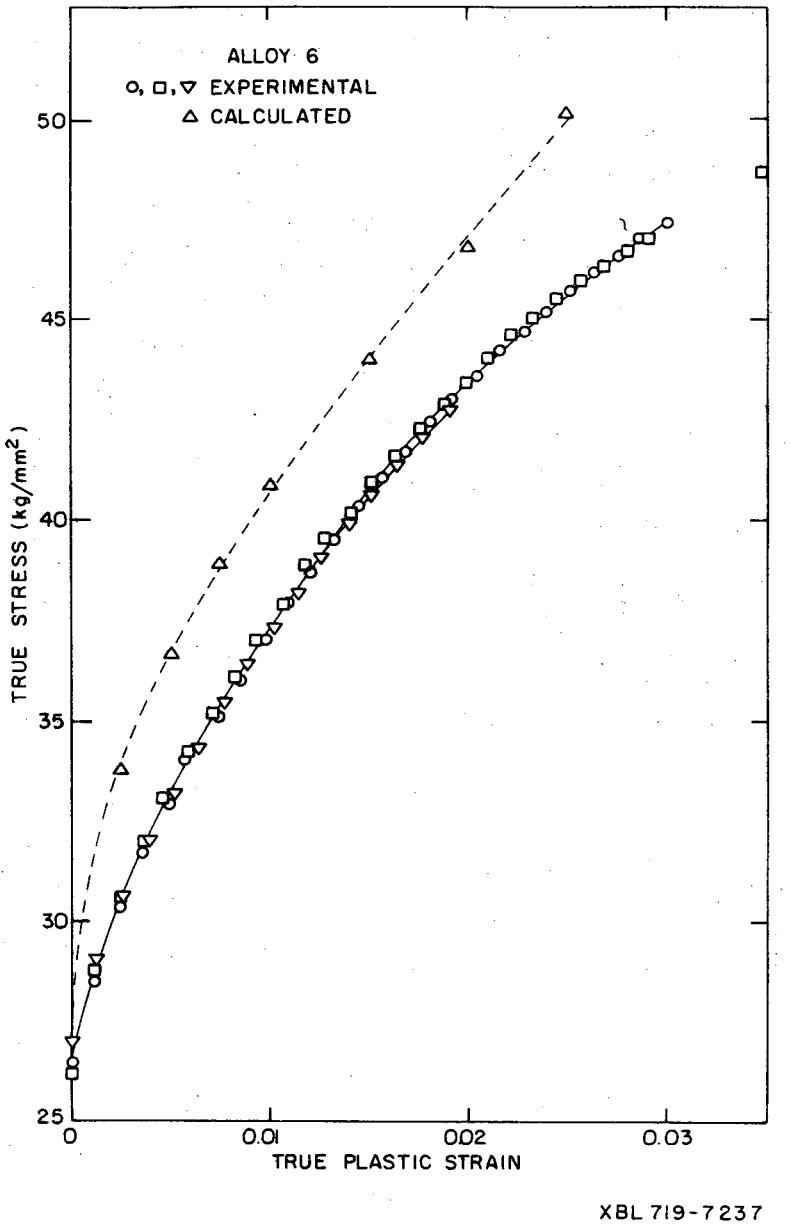

Fig. 18e.

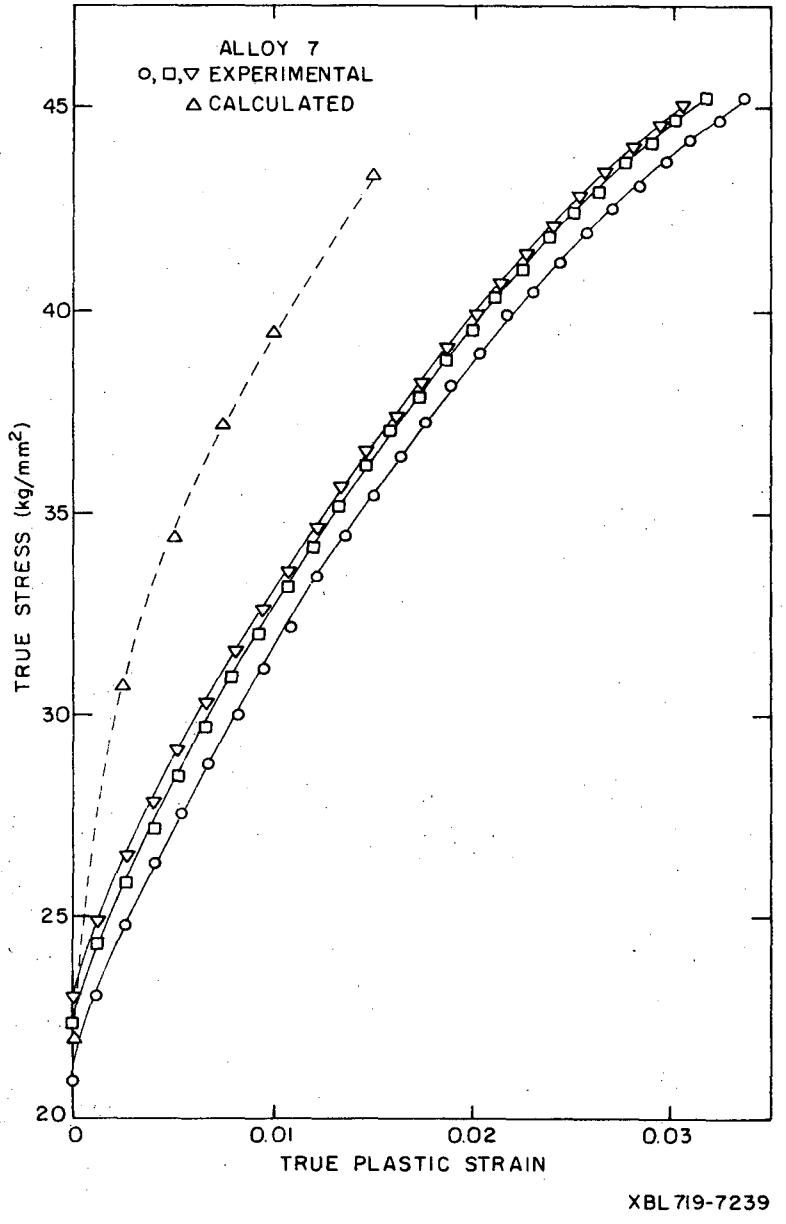

Fig. 18f.

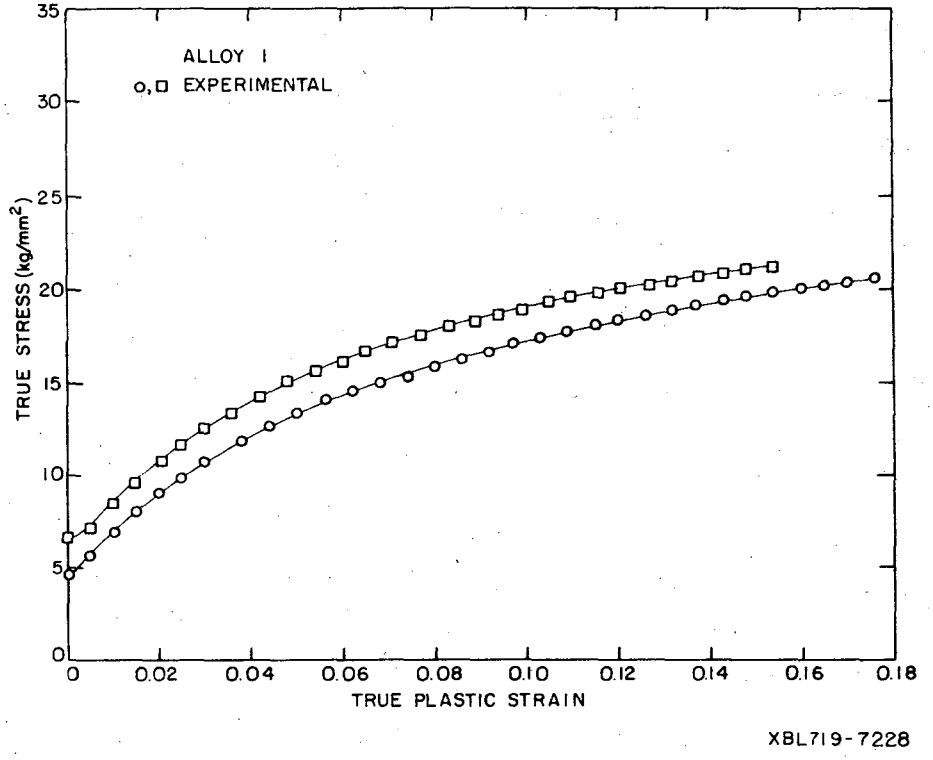

Fig. 19a.

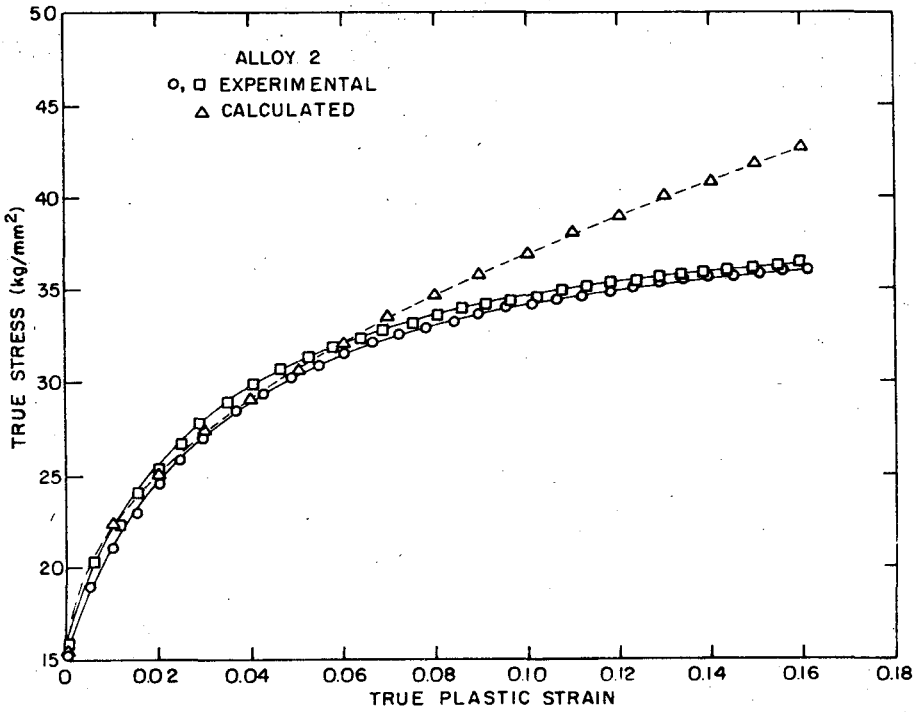

Fig. 19b.

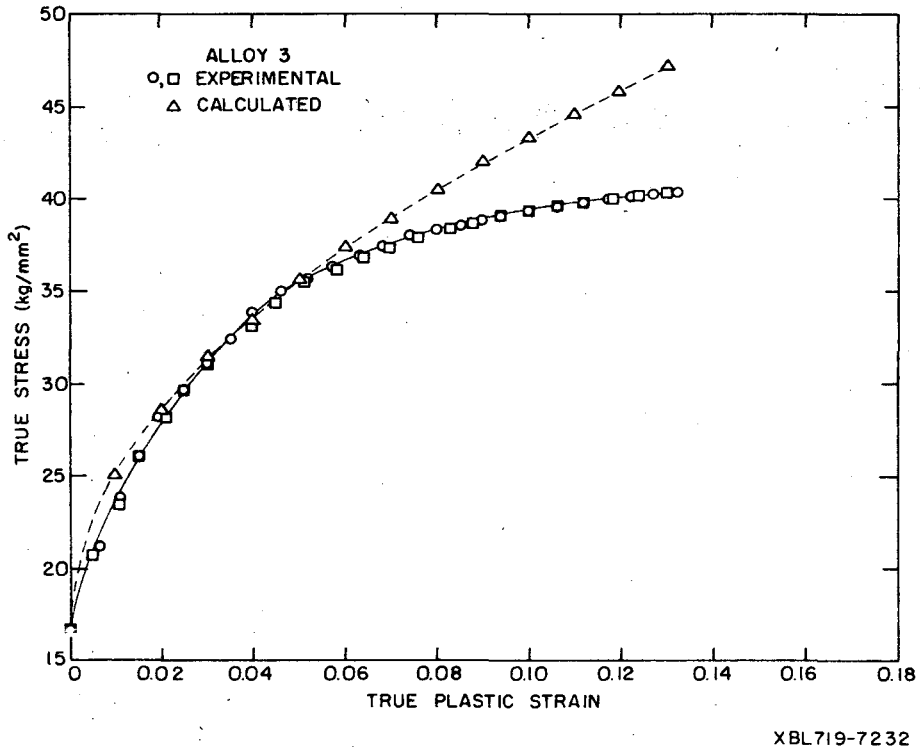

Fig. 19c.

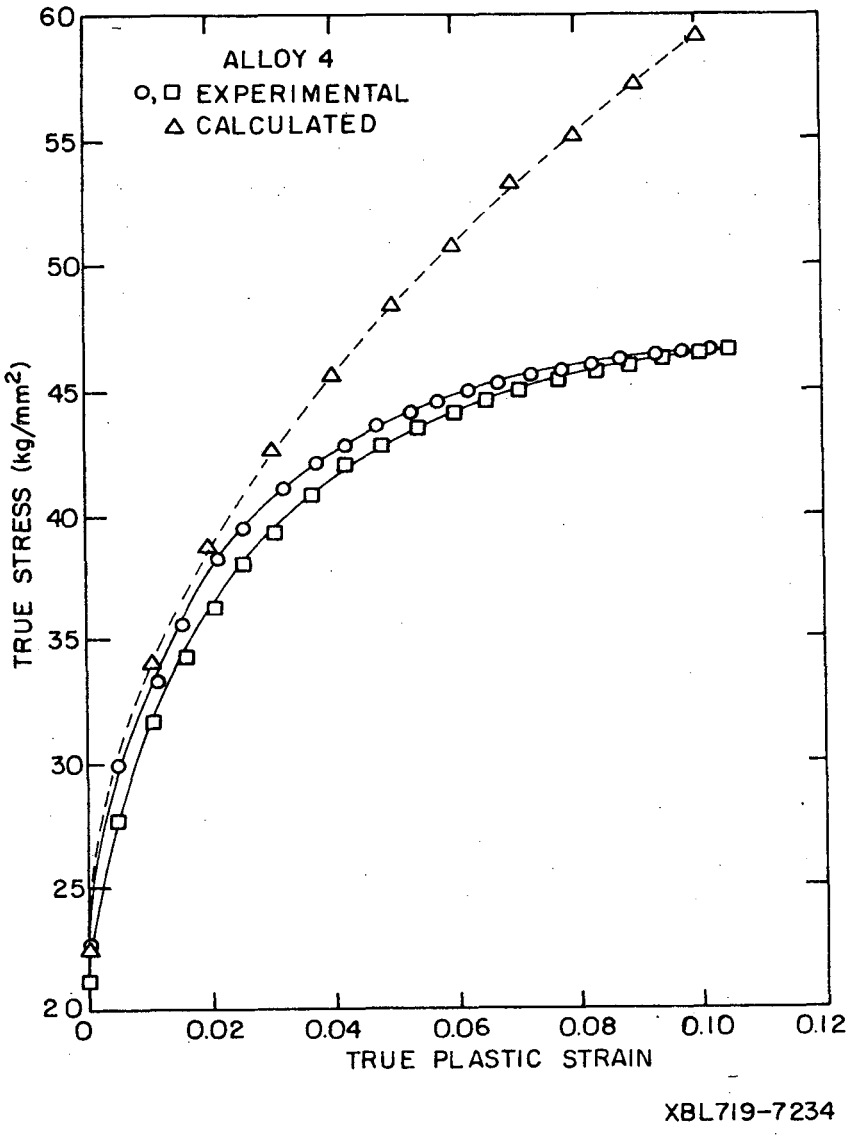

Fig. 19d.

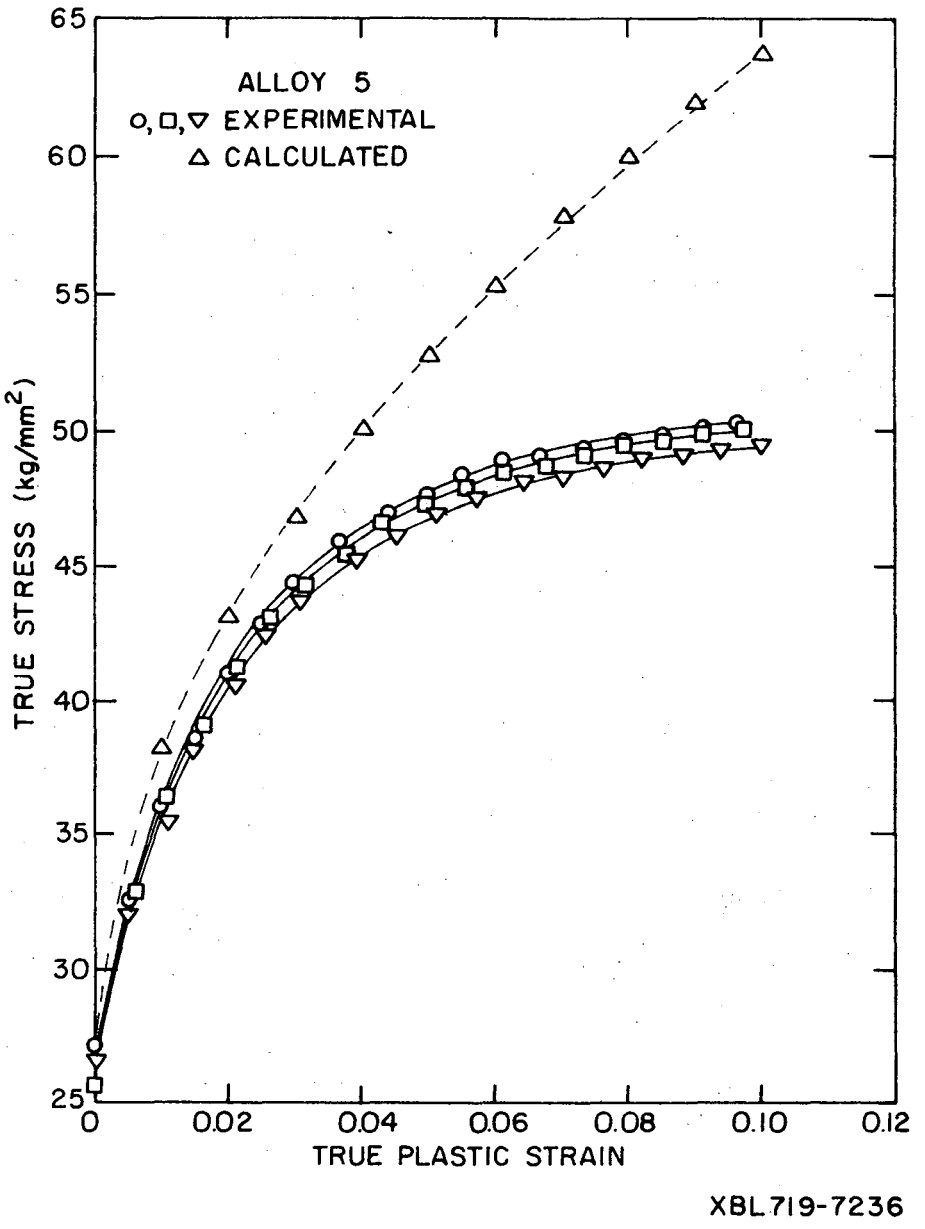

Fig. 19e.

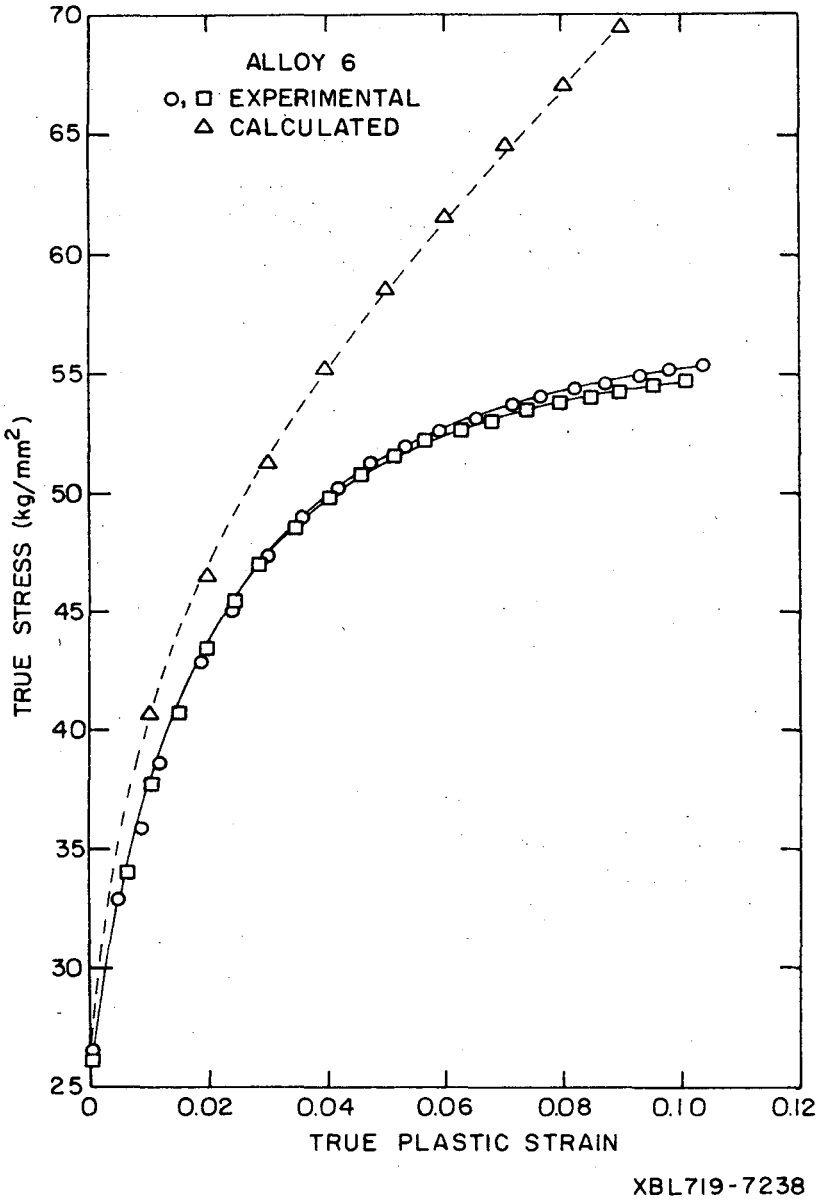

Fig. 19f.

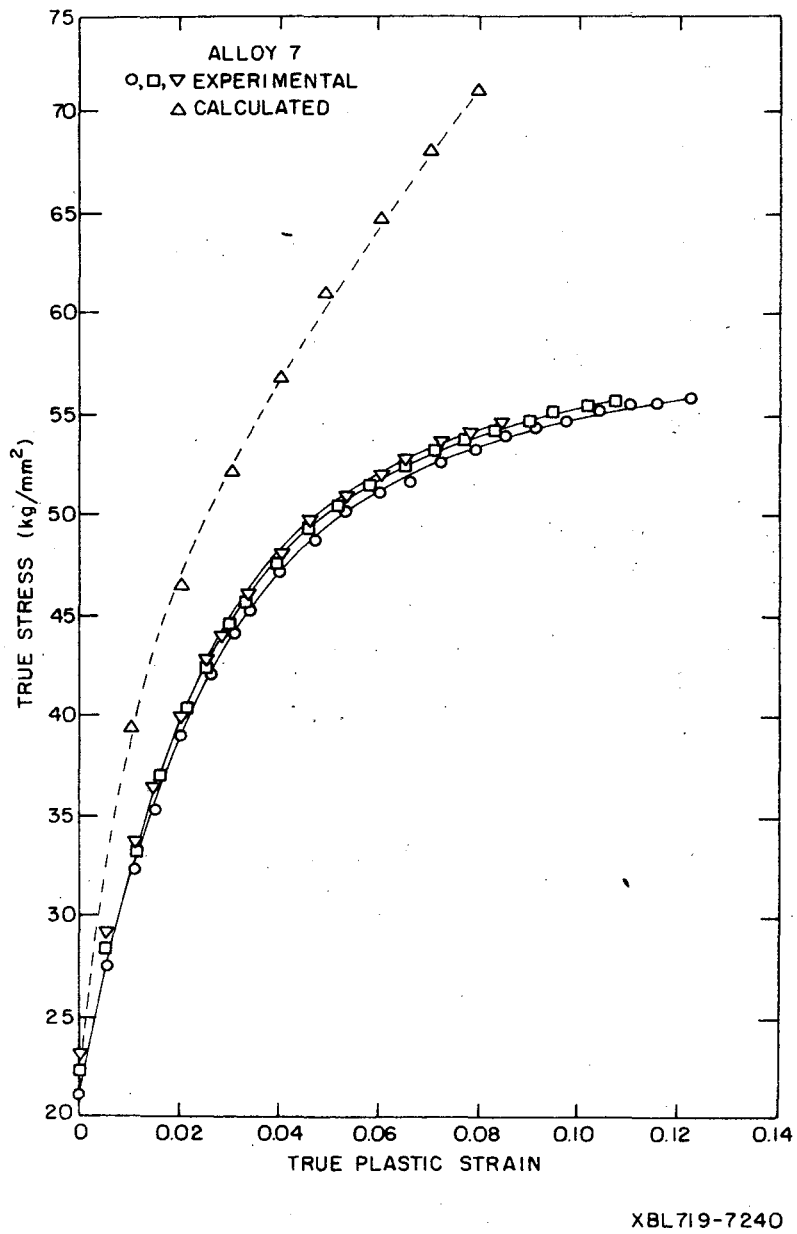

Fig. 19g.

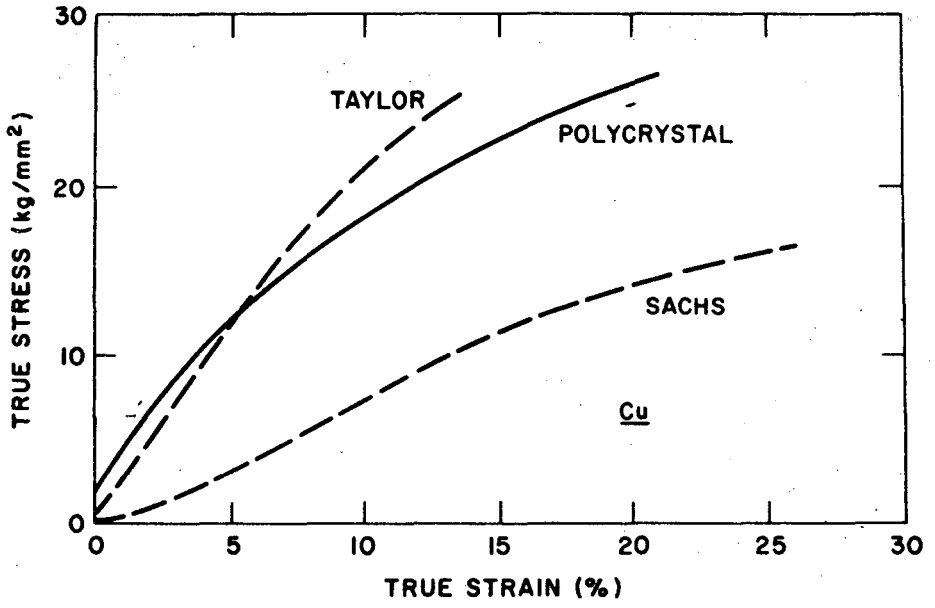

XBL 719-1471

Fig. 20.

TECHNICAL INFORMATION DIVISION
LAWRENCE BERKELEY LABORATORY
UNIVERSITY OF CALIFORNIA
BERKELEY, CALIFORNIA 94720